

**NIST Technical Note  
NIST TN 2284**

# **Pre-conceptual Design Activities of the NIST Neutron Source**

*Simulations of Neutron Beam Characteristics of the Proposed  
NIST Neutron Source*

Jeremy C. Cook  
Charles F. Majkrzak  
Hubert E. King

This publication is available free of charge from:  
<https://doi.org/10.6028/NIST.TN.2284>

**NIST Technical Note**  
**NIST TN 2284**

# **Pre-conceptual Design Activities of the NIST Neutron Source**

*Simulations of Neutron Beam Characteristics of the Proposed  
NIST Neutron Source*

Jeremy C. Cook  
*Research Facilities Operations  
NIST Center for Neutron Research*

Charles F. Majkrzak  
Hubert E. King  
*Neutron Condensed Matter Science  
NIST Center for Neutron Research*

This publication is available free of charge from:  
<https://doi.org/10.6028/NIST.TN.2284>

February 2024



U.S. Department of Commerce  
*Gina M. Raimondo, Secretary*

National Institute of Standards and Technology  
*Laurie E. Locascio, NIST Director and Under Secretary of Commerce for Standards and Technology*

NIST TN 2284  
February 2024

Certain commercial equipment, instruments, software, or materials, commercial or non-commercial, are identified in this paper in order to specify the experimental procedure adequately. Such identification does not imply recommendation or endorsement of any product or service by NIST, nor does it imply that the materials or equipment identified are necessarily the best available for the purpose.

#### **NIST Technical Series Policies**

[Copyright, Use, and Licensing Statements](#)

[NIST Technical Series Publication Identifier Syntax](#)

#### **Publication History**

Approved by the NIST Editorial Review Board on 2024-01-18

#### **How to Cite this NIST Technical Series Publication**

Cook JC, Majkrzak CF, King HE, (2024) Pre-conceptual Design Activities of the NIST Neutron Source: Simulations of Neutron Beam Characteristics of the Proposed NIST Neutron Source. (National Institute of Standards and Technology, Gaithersburg, MD), NIST Technical Note (TN) NIST TN 2284. <https://doi.org/10.6028/NIST.TN.2284>

#### **NIST Author ORCID iDs**

Jeremy C. Cook: 0000-0002-6348-1812

Charles F. Majkrzak: 0000-0002-9016-2008

Hubert E. King: 0000-0002-9536-3802

#### **Contact Information**

[jeremy.cook@nist.gov](mailto:jeremy.cook@nist.gov)

[charles.majkrzak@nist.gov](mailto:charles.majkrzak@nist.gov)

[hubert.king@nist.gov](mailto:hubert.king@nist.gov)

#### **Submit Comments**

[jeremy.cook@nist.gov](mailto:jeremy.cook@nist.gov)

100 Bureau Dr, MS 6103, Gaithersburg, MD, 20899, USA

## **Abstract**

This technical note is part of a series of notes describing preliminary analyses and planning for the pre-conceptual design of a reactor to replace, in due course, the National Bureau of Standards Reactor (NBSR) at the NIST Center for Neutron Research. The replacement reactor, namely the NIST Neutron Source (NNS), is currently planned to be a 20 Megawatts thermal power, pool-type compact core, cooled and moderated by light water (H<sub>2</sub>O) and fueled with low-enriched U-10Mo. The core comprises nine fuel assemblies in a three-by-three square lattice encased in a chimney. It is surrounded by a heavy water (D<sub>2</sub>O) filled reflector tank that contains two liquid deuterium (LD<sub>2</sub>) cold neutron sources on opposite sides of the core.

The report outlines preliminary studies undertaken to assess the thermal and cold neutron beam performance of a pre-conceptual design of the NNS. The results demonstrate the possibility and feasibility of significant performance enhancements of the NNS for a similar scale reactor core that builds on experience with the NBSR design. Further improvements and optimizations will be explored later as the NNS design evolves.

## **Keywords**

Cold Neutrons; Cold Neutron Sources; Neutron Guides; Neutron Research; Research Reactors; Thermal Neutrons.

## Table of Contents

<b>1. Introduction .....</b>	<b>1</b>
<b>2. CNS design and performance .....</b>	<b>3</b>
2.1. CNS cold neutron brightness.....	4
2.1.1. Effect of CNS location.....	5
2.1.2. Estimated CNS brightness gains with respect to NBSR (Unit 2 (LH <sub>2</sub> ) and Unit 3 (LD <sub>2</sub> ) CNS).....	5
2.1.3. Effect of CNS diameter on CNS brightness .....	9
2.1.4. Effect of a CNS cavity (re-entrant hole) on the CNS brightness in the beam direction.....	11
2.2. CNS size and neutron guide illumination .....	13
2.2.1. Optimization of CNS height .....	14
2.3. LD <sub>2</sub> CNS size and nuclear heat load .....	15
<b>3. Nuclear heating of aluminum substrate cold neutron in-pile guides .....</b>	<b>17</b>
<b>4. Thermal beams.....</b>	<b>18</b>
4.1. Thermal brightness and dependence on beam tube position.....	18
4.2. Performance of thermal neutron guides.....	20
<b>References.....</b>	<b>24</b>
<b>Appendix A - Review of Proposed Mark II LD2 CNS for OPAL: by Robert E. Williams.....</b>	<b>28</b>
<b>Appendix B - A preliminary analysis of the effect of CNS location on brightness, signal-to-noise ratio, and heat load (Authored by: Danyal J. Turkoglu).....</b>	<b>40</b>
<b>Appendix C - A visual of all NNS CNS diameters investigated in this work.....</b>	<b>45</b>
<b>Appendix D - Specific simulations for NCNR-NNS cold neutron current simulations (Version: October 17, 2022) .....</b>	<b>47</b>

## List of Tables

<b>Table 1. Integrals of the simulated neutron brightnesses shown in Figure 2 for all neutron wavelengths and for cold neutrons with <math>\lambda \geq 4\text{\AA}</math>.....</b>	<b>7</b>
<b>Table 2. Estimated transmittable neutron currents entering the cold neutron guide networks for the NBSR Unit 2 CNS (LH<sub>2</sub>) versus the NNS CNS with 6 cm × 15 cm guide entrances .....</b>	<b>8</b>
<b>Table 3. Estimated transmittable neutron currents entering the cold neutron guide networks for the NBSR Unit 2 CNS (LH<sub>2</sub>) versus the NNS CNS with 6 cm × 20 cm guide entrances .....</b>	<b>8</b>
<b>Table 4. Estimated transmittable neutron currents entering the cold neutron guide networks for the NBSR Unit 3 CNS (LD<sub>2</sub>) versus the NNS CNS with 6 cm × 15 cm guide entrances .....</b>	<b>9</b>
<b>Table 5. Estimated transmittable neutron currents entering the cold neutron guide networks for the NBSR Unit 3 CNS (LD<sub>2</sub>) versus the NNS CNS with 6 cm × 20 cm guide entrances .....</b>	<b>9</b>
<b>Table 6. Summary of total heating contributions due to various radiation components and total minimum cryogenic heat loads for NNS CNS as a function of CNS diameter. These values do not include the non-nuclear heat which is estimated to be about 10% in addition .....</b>	<b>15</b>

## List of Figures

Figure 1. Schematic Showing Access to the Two Cold Neutron Sources and Thermal Beam Tubes.....	2
Figure 2. MCNP simulations of the cold neutron brightness spectrum of the NBSR LH <sub>2</sub> Unit 2 CNS (red curve), Unit 3 CNS (dark blue curve), and the NNS CNS (light blue curve cavity side, dark green curve non-cavity side). .....	7
Figure 3. Comparison of the core thermal flux distributions of the NBSR and NNS. ....	8
Figure 4. Simulated usable CNS brightness as a function of neutron wavelength for NNS CNS models with various LD <sub>2</sub> vessel diameters indicated in the legend and for the current NBSR Unit 2 LH <sub>2</sub> CNS and the future NBSR Unit 3 LD <sub>2</sub> CNS (see legend). The reference OPAL-like (∅ 30 cm) CNS model is represented by solid black circles. ....	10
Figure 5. NNS CNS neutron brightness ratios with respect to the present NBSR LH <sub>2</sub> Unit 2 CNS brightness (obtained from the results shown in Figure 4) for the NNS LD <sub>2</sub> vessel diameters indicated in the legend. The reference OPAL-like (∅ 30 cm) CNS model is represented by solid black circles. ....	10
Figure 6. NNS CNS neutron brightness ratios with respect to the future NBSR LD <sub>2</sub> Unit 3 CNS brightness (obtained from the results shown in Figure 4) for the NNS LD <sub>2</sub> vessel diameters indicated in the legend. The reference OPAL-like (∅ 30 cm) CNS model is represented by the solid black circles. ....	11
Figure 7. Plan view through the center of the current MCNP model showing the CNS with one cavity. ....	12
Figure 8. Simulated neutron brightness gain from viewing the cavity side of the CNS in the current model as opposed to the non-cavity side (ratio of light blue to dark green curves in Figure 2). ....	13
Figure 9. A schematic representation of full-illumination (top) and under-illumination (bottom) of an ideal, long, straight neutron guide. “Long” in this context is for wavelengths satisfying $W/L < \theta_c$ . ....	13
Figure 10. Simulated origins of neutrons on a rectangular cross-section source that are transmitted to the exit of group #3, guide #4 described in Ref. [5] for several neutron wavelengths. ....	14
Figure 11. Dependence of the CNS cryogenic system radiation heat load vs. model CNS vessel diameter. The Al-6061 layer thicknesses for each model are assumed unchanged from the current (∅ 30 cm) model values. ....	16
Figure 12. Estimated nuclear heating per unit mass ( $Wg^{-1}$ ) for Al-substrate in-pile cold neutron guides with entrances 1.5 m from the center of the CNS and 20 MW reactor power. The red curve is gamma heating, the green curve is saturation-level <sup>28</sup> Al-decay $\beta$ , the blue curve is neutron, and the black curve is the total heating. ....	17
Figure 13. Plan view through the fuel center of the reactor core. The thermal neutron brightness spectrum was tallied at the position indicated by the blue circle on the larger thermal tube to the upper right. ....	19
Figure 14. Simulated thermal neutron brightness vs. neutron wavelength for the NNS (red points) at the position indicated by the blue dashed circle in Figure 13. The wintergreen colored points are similar simulations for the NBSR BT6 beam at the shield exit. The solid curves are Maxwellian fits. A fitted effective temperature of 317 K for the NNS indicates that the contributing spectrum is well-thermalized. ....	20

**Figure 15. Plan view showing thermal beam tubes. The beam tube penetrates the biological shield (dark green) and is large enough to accommodate a 6 cm(w) × 20 cm (h) thermal neutron guide. The 6 cm × 20 cm thermal guides are assumed to start at the entrance to the biological shield (blue dashed circle). .....22**

**Figure 16. Center column: Simulated thermal neutron intensities (flux per unit wavelength) as a function of neutron wavelength on a 6 cm(w) × 20 cm (h) target at a distance  $d$  (m) from the exit of the biological shield. Black curves: Through the empty 15 cm(w) × 25 cm(h) biological shield penetration. Red curves: At the exit of a 6cm × 20cm thermal neutron guide starting at the entrance to the biological shield. The corresponding guide gains (ratio of red to black curves) are shown in the right-hand column. ....23**

## **Acknowledgments**

The authors would like to acknowledge the team of individuals working on the design, including current members from the NCNR, active contributors outside the NCNR, and past contributors. The names are listed in alphabetical order.

### **Current NCNR Members**

Osman Ş. Çelikten, Jeremy C. Cook, David J. Diamond, Anil Gurgen, John M. Jurns, Hubert E. King, Charles F. Majkrzak, Thomas H. Newton, Dağistan Şahin, Joy S. Shen, Abdullah G. Weiss

### **Active Contributors**

#### **Brookhaven National Laboratory, Nuclear Science and Technology Department**

Lap-Yan Cheng, Arantxa Cuadra, Peter Kohut, Cihang Lu, Athi Varuttamaseni

#### **Shimon Peres Negev Nuclear Research Center**

Idan R. Baroukh, Eliezer Nahmani, Yaniv Shaposhnik

#### **NIST, Engineering Laboratory, Structures Group**

DongHun Yeo

### **Past Contributors**

Patrick Park (*currently affiliated with Princeton University*)

Danyal Turkoglu (*currently affiliated with USNC-Tech*)

Robert E. Williams

Zeyun Wu (*currently affiliated with Virginia Commonwealth University*)

### **Interns**

Duncan Beach, Evan Bures, Amir Dajani, Patrick Park



## 1. Introduction

In contrast to power reactors, research reactors usually have a compact core-fuel region surrounded by an extensive moderator/ reflector to produce uncluttered, accessible zones of highly-thermalized neutron flux outside the fuel. These regions are “tapped” into neutron beams directed toward the instruments surrounding the reactor. These neutron beams are the primary output of the research reactor as opposed to heat for steam generation, which is the desired output of the power reactor core. As such, these neutron beams constitute desirable leakage from the core, and the compact core design allows the reactor to maintain criticality with low enrichment fuel of appropriate density.

This report describes preliminary assessments of cold and thermal neutron beams for a NIST replacement research reactor, referred to as the NIST Neutron Source (NNS). Cold and thermal neutrons possess unique characteristics for measurements of the structure, dynamics, and magnetic properties of condensed matter. Thermal neutrons are typically characterized by a room-temperature Maxwellian energy distribution, which peaks around 0.025 eV with Debroglie wavelengths in the 0.1 nm range. Cold neutrons have lower effective Maxwellian temperatures, sometimes in the 10's of Kelvin range, and their generation requires a dedicated Cold Neutron Source (CNS). Neutrons are transported from the core to the scientific instruments via beam tubes. The current plan incorporates two liquid deuterium (LD<sub>2</sub>) cold neutron sources and up to eight thermal beam tubes in the heavy water (D<sub>2</sub>O) reflector surrounding the reactor core, as shown in Figure 1.

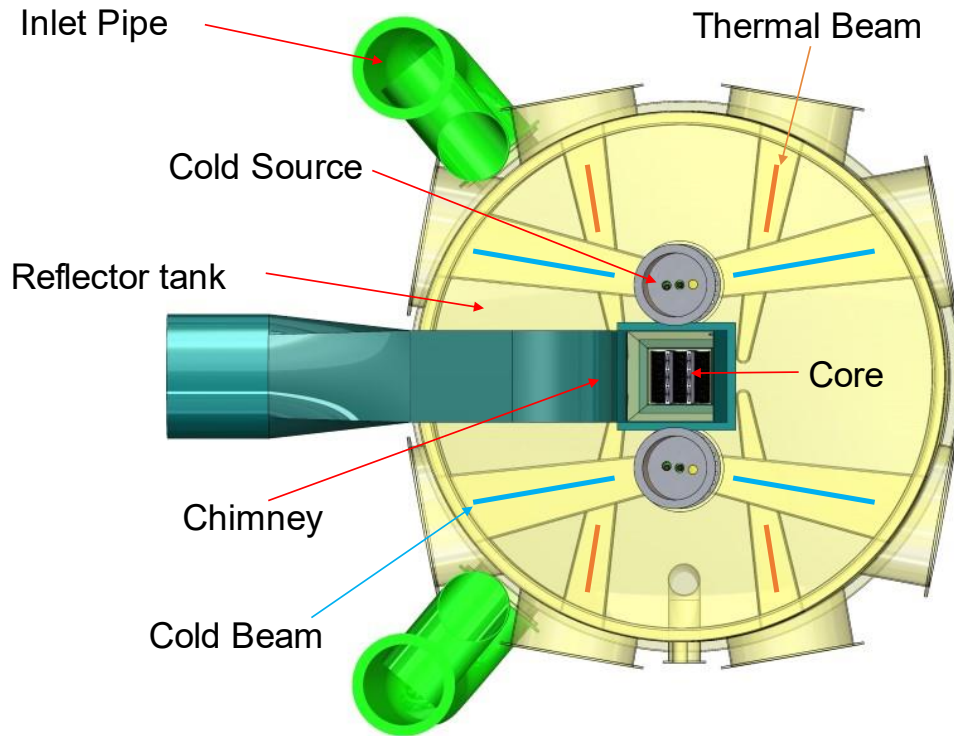


**Figure 1. Schematic showing access to the two cold neutron sources and thermal beam tubes, possibly located at different elevations. The red and blue lines indicate the relative temperature of the neutron beams, not physical structures.**

## 2. CNS design and performance

To meet future research demands, the NNS [1–4] must provide high-performance cold neutron beams, thermal neutron beams, and irradiation locations exceeding the experimental capacity of the existing NBSR with respect to quantity and quality [5]. The number of beams must exceed the existing facilities to accommodate current overbooking. Furthermore, the “signal-to-noise” ratio (SNR), i.e., the quality of the beams, must meet or exceed existing neutron beams with minimal epithermal and fast neutron contamination. The CNS usually comprises a localized region of cryogenically-cooled moderator placed in or near the peak of the unperturbed thermal neutron flux in the moderator/ reflector of a reactor (or near the target/moderator of a pulsed neutron source) [6], [7], [8]. Its objective is to shift the thermal Maxwellian neutron flux distribution towards lower energies (lower temperatures).

The optimum cold moderator depends on the functional application. Long-pulse spallation neutron sources have favored para ( $H_2$  molecule with antiparallel proton spins) liquid hydrogen ( $LH_2$ ) with a reflector and cold moderator that may be separated by a thermal neutron absorbing layer (decoupled), which sharpens the pulse shape [9] [10]. Since para hydrogen is the molecular ground state, a high para- $H_2$  fraction is desirable for cold neutron production below 50 meV [9] [11] [12] [13]. The para-to-ortho spin-flip transition results in a 14.7 meV downscatter of the neutron, whereas a scatter from ortho hydrogen results in a 14.7 meV neutron energy gain. In the absence of radiation, the para content in  $LH_2$  increases by natural conversion even without a catalyst; however, the presence of neutron and gamma radiation produces an increased fraction of ortho hydrogen [14]. Measurements on the current (Unit 2) NBSR  $LH_2$  cold source, which is not catalyzed, showed consistency with an equilibrium ortho to para  $H_2$  ratio of 17.5% to 82.5%, respectively, while the reactor operates at 20 MW [15].

Some recent research reactor CNS designs have trended towards liquid deuterium ( $LD_2$ ) (typically operating between temperatures between 23 K to 25 K) moderators [16] [17] [18] [19] [20] [21] rather than liquid hydrogen [22]. This is because deuterium has a relatively higher moderating ratio than hydrogen due to its lower absorption cross-section. However, significantly larger moderator volumes are required because of the much smaller deuterium scattering cross-section. The ground state of  $D_2$  is ortho in contrast to  $H_2$  (para) and the degeneracies of the respective states (6 symmetric, 3 antisymmetric) lead to a high-temperature limit 2:1 ortho:para ratio. The desired neutron energy loss process for  $D_2$  is an ortho-to-para spin flip, favoring a high ortho fraction. However, the presence of para deuterium in the  $LD_2$  has relatively less influence than that of ortho hydrogen in  $LH_2$ . This is because the thermal-cold neutron scattering cross-sections of ortho and para  $D_2$  are similar, whereas the scattering cross-section of ortho-hydrogen is significantly larger than the para cross-section for neutron energies below about 65 meV (or neutron wavelengths,  $\lambda$ , greater than about 0.1 nm (1 Å)) [23]. The presence of ortho- $H_2$  is correspondingly more detrimental for  $LH_2$  cold sources. Ageron [16] observed that introducing a re-entrant hole or cavity into the liquid volume may enhance the cold neutron flux in the direction of the cold neutron guides and that introducing about 10 %  $LH_2$  with an ortho:para ratio of 50:50 could potentially enhance the cold neutron flux by about 20 %. Controlling the ortho-para concentration in a high radiation field is difficult and impractical, whereas obtaining a high para fraction may be readily achieved with a suitable

catalyst. The overall performance of the source can be estimated via Monte Carlo techniques for various ortho-para ratios, provided reliable ortho and para scattering kernel data is available. In the present Monte Carlo N-Particle code (MCNP)<sup>1</sup> transport simulations of LD<sub>2</sub>, 19 K scattering kernels for LD<sub>2</sub> are used [24] with an LD<sub>2</sub> void fraction of about 10 %, although the use of natural thermosyphon would increase the deuterium temperature to about 23 K. The ortho-para ratio in the MCNP model is 2:1, which also corresponds to the high-temperature quantum mechanical limit. It is based on measurements under radiation performed at the PSI spallation neutron source in Switzerland [25] and is the basis of the MCNP models for the Unit 3 CNS at the NBSR [21] and the NNS CNS. The actual ortho content may be higher due to increased radiation-induced dissociation and recombination of the D<sub>2</sub> molecules in the NBSR and NNS sources with respect to the PSI CNS. Energy deposition considerations predict more like a 3:1 ratio; however, a 2:1 ratio should be conservative for CNS performance simulations.

The current NNS CNS model is similar to the OPAL CNS design, in which the liquid deuterium (LD<sub>2</sub>) moderator is maintained in a single liquid phase while still operating under thermosyphon rather than relying on a deuterium pump or circulator [26], [27], [28], [29]. A detailed review of the OPAL CNS is provided in **Appendix A**. The LD<sub>2</sub> moderator is maintained in single-phase by directly cooling the in-pile vessel in a double-skinned arrangement with a helium inlet temperature of about 19 K. Helium maintains the LD<sub>2</sub> subcooled without boiling. One disadvantage of this design is the increased double-skin material and the increased heat load. However, a significant advantage of the proposed system is the ability to maintain the reactor at full power without overheating the vessel material in the event of an LD<sub>2</sub> boil-off resulting from the loss of one of the two He compressors (**Appendix A**). Currently, the NNS model has two identical LD<sub>2</sub> sources, although the possibility of having dissimilar CNSs optimized differently for different instrument requirements is not excluded. A fixed-diameter CNS thimble may be employed with any residual space surrounding a smaller-diameter CNS filled with D<sub>2</sub>O reflector. The CNS design will be simplified to achieve the highest operational reliability and stability.

## 2.1. CNS cold neutron brightness

The primary function of the NNS facility is to support neutron science; therefore the CNS spectrum is of primary importance. The following sections explore various parameters related to CNSs. There are diverse definitions of what constitutes an upper energy limit for cold neutrons. However, an early definition, adopted by Webb [7], has cold neutrons with energies less than 0.005 eV ( $\lambda$  greater than about 4 Å). We adopt this definition since cold neutron instruments largely exploit greater than 4 Å incident energy neutrons. Note that published work associated with cold neutron production at the OPAL reactor [26], [29] refers to cold neutron

---

<sup>1</sup> MCNP® and Monte Carlo N-Particle® are registered trademarks owned by Triad National Security, LLC, manager and operator of Los Alamos National Laboratory. Any third party use of such registered marks should be properly attributed to Triad National Security, LLC, including the use of the ® designation as appropriate. Any questions regarding licensing, proper use, and/or proper attribution of Triad National Security, LLC marks should be directed to [trademarks@lanl.gov](mailto:trademarks@lanl.gov). Its identification in this report does not reflect any endorsements by NIST or the US Department of Commerce.

energies less than 10 meV ( $\lambda > 2.9 \text{ \AA}$ ), necessitating caution when comparing published cold neutron flux values between facilities.

### 2.1.1. Effect of CNS location

The cold neutron brightness was evaluated at the proposed neutron guide entrances (assumed 1.5 m distant from the CNS center). Defining the cold neutron spectrum SNR as the ratio of flux with neutron wavelengths greater than 1  $\text{\AA}$  to that for neutrons with wavelengths less than 1  $\text{\AA}$ , it was determined that moving the CNS closer to the core for increased cold neutron brightness comes at the expense of increased nuclear heat load and reduced SNR. It was concluded that placing the CNS z-axis at ( $x = \pm 45 \text{ cm}$ ,  $y = 0 \text{ cm}$ ) with respect to the fuel origin offered a good compromise between SNR, cold neutron gain, and manageable heat load. These are the CNS vertical axis locations in the present reactor core model with a default CNS diameter of 30 cm. A preliminary version of this analysis by D. Turkoglu is available in **Appendix B**.

### 2.1.2. Estimated CNS brightness gains with respect to NBSR (Unit 2 (LH<sub>2</sub>) and Unit 3 (LD<sub>2</sub>) CNS)

Without optimizing the brilliance transfer to a suite of instruments of uncertain configuration, a reproducible figure-of-merit (FOM) for the cold neutron gain at the instruments is the total cold neutron currents within a usable divergence range at the combined guide entrances. Liouville's theorem [30] states that, for a conservative system, the phase-space density along the trajectories of the system is constant. In the context of beam transport, this means that the current per unit phase space (area, divergence, wavelength, time), i.e., brightness, evaluated anywhere along the beam will be the same as at the source in a lossless system. This is the source brightness that could be theoretically transferred to an instrument in a lossless system, and the currents are this value multiplied by the guide entrance areas. Thus, the theoretical gain is the ratio of these quantities for the NNS compared with the NBSR. Practical factors that reduce these upper limits are reflection losses, material transmission losses in the neutron guide and beam transfer system, and under-illumination of the neutron guide entrances (see Sec. 2.2) and the sample. MCNP simulations of the CNS cold neutron brightness (cavity side - see Sec. 2.1.4) were compared with those for the NBSR Unit 2 (LH<sub>2</sub>) [22] and Unit 3 (LD<sub>2</sub>) [21] models. The cold neutron brightness is not isotropic; therefore, the concept of a *usable* divergence range (characterized by  $\mu = \cos\theta \geq 0.99875$  [ $\theta \leq 50 \text{ mrad} \approx 2.9^\circ$ ]) in the direction of the cold neutron guide tube entrances was developed. This specific angular range corresponds to the limiting divergence angle of a straight-sided, all  $m=2$  supermirror neutron guide for a neutron wavelength of about 0.1 nm (10  $\text{\AA}$ ). For larger values of  $\mu$ , the brightness varies only slightly in the direction of the neutron guide entrances. To obtain the brightness in units of  $\text{cm}^{-2}\text{s}^{-1}\text{MeV}^{-1}\text{sr}^{-1}$ , the MCNP tally was normalized by multiplying by the number of fission neutrons produced per second at 20 MW (equates to  $1.525 \times 10^{18} \text{ s}^{-1}$ ) and dividing by the area of the tally (in this case  $6 \text{ cm} \times 15 \text{ cm} = 90 \text{ cm}^2$ ) and by the difference in the solid angle ( $\Delta\Omega$ ) represented in Eq. (1), which in this case would equate to  $2\pi \times (1 - 0.99875)$ . In this way, the current tally representing the bin encompassing  $\mu$  in the range of  $0.99875 \rightarrow 1$  is obtained directly in the units of  $\text{cm}^{-2}\text{s}^{-1}\text{MeV}^{-1}\text{sr}^{-1}$ . Conversion to units of  $\text{cm}^{-2}\text{s}^{-1}\text{\AA}^{-1}\text{sr}^{-1}$  is performed via the

Jacobian  $J$  in Eq. (2), where  $m_n$  is the neutron mass,  $E_n$  is the neutron energy, and  $h$  is Planck's constant.

$$\Delta\Omega = 2\pi\Delta\mu \quad (1)$$

$$J = 2 \frac{\sqrt{2m_n E_n^3}}{h} \quad (2)$$

The cold neutron threshold denotes neutron wavelengths greater than 0.4 nm (4 Å) (neutron energies < 5 meV) - see Sec. 1. The results are shown in Figure 2. The integral NNS CNS brightness (cavity side) is about  $1.81 \times 10^{13} \text{ cm}^{-2}\text{s}^{-1}\text{sr}^{-1}$ , and the integrals for  $\lambda \leq 0.5 \text{ Å}$  and  $\lambda \leq 1 \text{ Å}$  are  $1.45 \times 10^{12} \text{ cm}^{-2}\text{s}^{-1}\text{sr}^{-1}$  (about 8% of the total) and  $2.39 \times 10^{12} \text{ cm}^{-2}\text{s}^{-1}\text{sr}^{-1}$  (about 13% of the total), respectively. The corresponding total and cold neutron spectrum integrals are summarized in **Table 1**, indicating cold neutron brightness gains of about 3.48 and 2.64 with respect to the present NBSR LH<sub>2</sub> Unit 2 and the future LD<sub>2</sub> Unit 3 CNS, respectively.

The simulated brightness gains in Table 1 (for equivalent 20 MW operating power) are better understood by examining the core thermal flux distributions (Figure 3). The compact core of the NNS produces a peak thermal neutron flux in the reflector outside of the fuel region, whereas the NBSR core thermal flux peaks at the center of the fuel, which is inaccessible to thermal beam and cold neutron source thimbles. The thermal flux distribution of the NNS alone allows the thimbles to be placed much more optimally in the thermal flux peak. The NNS core will produce a minimum peak unperturbed thermal neutron flux in the reflector of about  $5 \times 10^{14} \text{ cm}^{-2}\text{s}^{-1}$  at 20 MW. For the NBSR, the beam thimbles are located at a radius where the unperturbed thermal neutron flux has fallen to about  $2 \times 10^{14} \text{ cm}^{-2}\text{s}^{-1}$  at 20 MW power.

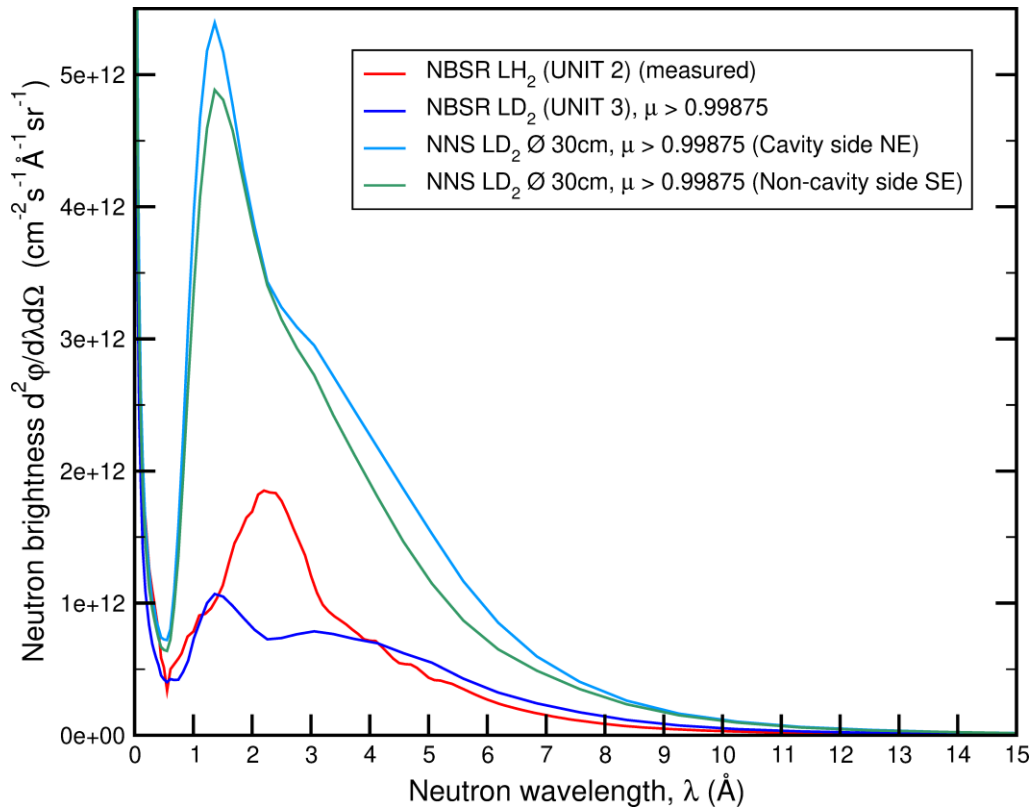


Figure 2. MCNP simulations of the cold neutron brightness spectrum of the NBSR LH<sub>2</sub> Unit 2 CNS (red curve), Unit 3 CNS (dark blue curve), and the NNS CNS (light blue curve cavity side, dark green curve non-cavity side).

Table 1. Integrals of the simulated neutron brightnesses shown in Figure 2 for all neutron wavelengths and for cold neutrons with  $\lambda \geq 4\text{\AA}$ .

BRIGHTNESS INTEGRALS FOR CNS ( $\text{cm}^{-2}\text{s}^{-1}\text{sr}^{-1}$ ) ( $\mu > 0.99875$ at guide entrance)					
Wavelength range ( $\text{\AA}$ )	NBSR Unit 2 LH <sub>2</sub>	NBSR Unit 3 LD <sub>2</sub>	NNS LD <sub>2</sub> ( $\emptyset$ LD <sub>2</sub> = 30 cm, cavity side)	Ratio NNS/NBSR Unit 2 LH <sub>2</sub>	Ratio NNS/NBSR Unit 3 LD <sub>2</sub>
0→60	$6.99 \times 10^{12}$	$5.65 \times 10^{12}$	$1.81 \times 10^{13}$	2.59	3.20
4→60	$1.44 \times 10^{12}$	$1.90 \times 10^{12}$	$5.01 \times 10^{12}$	3.48	2.64

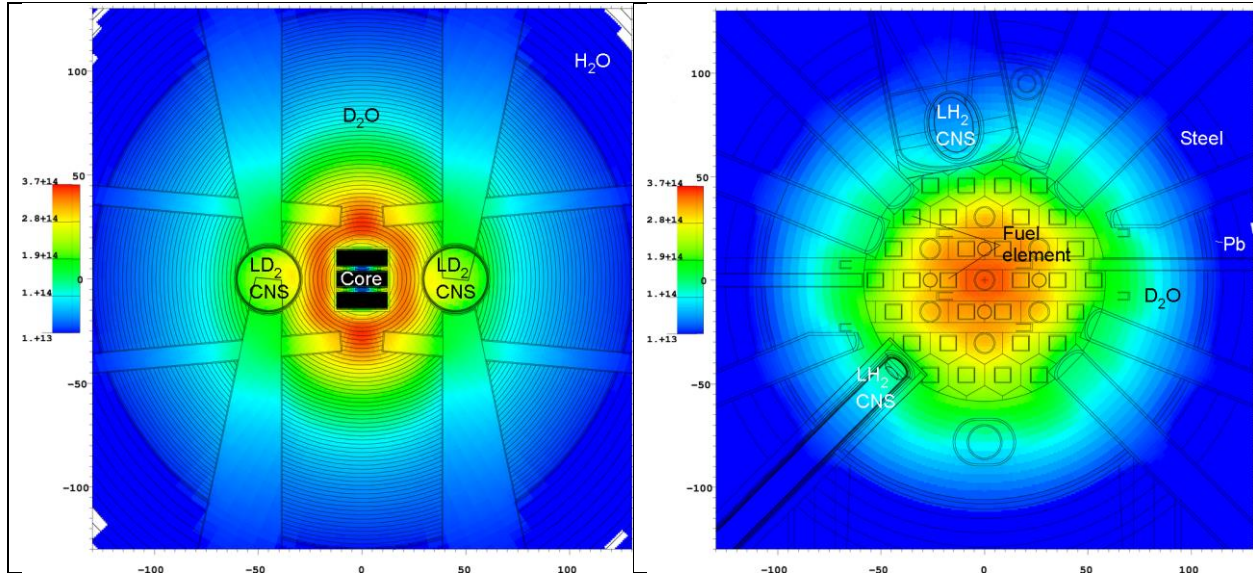


Figure 3. Comparison of the core thermal flux distributions of the NBSR and NNS.

The cold neutron current FOMs have been evaluated for the 12 NBSR guide entrances illuminated by the Unit 2 and Unit 3 CNSs and for the 16 NNS guide entrances placed 1.5 m from the CNS center. The results for 6 cm × 15 cm NNS cold neutron guide entrances are summarized in **Table 2** and **Table 4** with respect to Unit 2 and Unit 3, respectively. The corresponding values for 6 cm × 20 cm NNS cold neutron guide entrances are given in **Table 3** and **Table 5**, respectively). Specific simulations from which these quantities are obtained are given in the tables in **Appendix C**.

Table 2. Estimated transmittable neutron currents entering the cold neutron guide networks for the NBSR Unit 2 CNS (LH<sub>2</sub>) versus the NNS CNS with 6 cm × 15 cm guide entrances

Cold Source	$J_{tot}$ (all $\lambda$ ) ( $s^{-1}$ )	$J_{tot}$ (cold neutrons $\lambda \geq 0.4$ nm) ( $s^{-1}$ )
NBSR LH <sub>2</sub> Unit 2 (all cold guides)	$3.0 \times 10^{13}$	$6.3 \times 10^{12}$
NNS (6 cm × 15 cm) (16 equivalent guide entrances)	$2.3 \times 10^{14}$	$5.8 \times 10^{13}$
Gain NNS/NBSR Unit 2	7.5	9.2

Table 3. Estimated transmittable neutron currents entering the cold neutron guide networks for the NBSR Unit 2 CNS (LH<sub>2</sub>) versus the NNS CNS with 6 cm × 20 cm guide entrances

Cold Source	$J_{tot}$ (all $\lambda$ ) ( $s^{-1}$ )	$J_{tot}$ (cold neutrons $\lambda \geq 0.4$ nm) ( $s^{-1}$ )
NBSR LH <sub>2</sub> Unit 2 (all cold guides)	$3.0 \times 10^{13}$	$6.3 \times 10^{12}$
NNS (6 cm × 20 cm) (16 equivalent guide entrances)	$2.8 \times 10^{14}$	$7.0 \times 10^{13}$
Gain NNS/NBSR Unit 2	9.1	11.1



**Table 4. Estimated transmittable neutron currents entering the cold neutron guide networks for the NBSR Unit 3 CNS (LD<sub>2</sub>) versus the NNS CNS with 6 cm × 15 cm guide entrances**

Cold Source	$J_{tot}$ (all $\lambda$ ) (s <sup>-1</sup> )	$J_{tot}$ (cold neutrons $\lambda \geq 0.4$ nm) (s <sup>-1</sup> )
NBSR LD <sub>2</sub> Unit 3 (all cold guides)	$4.0 \times 10^{13}$	$1.4 \times 10^{13}$
NNS (6 cm × 15 cm) (16 equivalent guide entrances)	$2.3 \times 10^{14}$	$5.8 \times 10^{13}$
Gain NNS/NBSR Unit 3	5.7	4.2

**Table 5. Estimated transmittable neutron currents entering the cold neutron guide networks for the NBSR Unit 3 CNS (LD<sub>2</sub>) versus the NNS CNS with 6 cm × 20 cm guide entrances**

Cold Source	$J_{tot}$ (all $\lambda$ ) (s <sup>-1</sup> )	$J_{tot}$ (cold neutrons $\lambda \geq 0.4$ nm) (s <sup>-1</sup> )
NBSR LD <sub>2</sub> Unit 3 (all cold guides)	$4.0 \times 10^{13}$	$1.4 \times 10^{13}$
NNS (6 cm × 20 cm) (16 equivalent guide entrances)	$2.8 \times 10^{14}$	$7.0 \times 10^{13}$
Gain NNS/NBSR Unit 3	7.0	5.2

The cold neutron gains in Table 2 to Table 5 are approximately the products of the cold neutron ( $\lambda \geq 0.4$  nm) brightness gains from Table 1 (3.48 (Unit 2) and 2.64 (Unit 3)), the guide entrance solid angle ratios with respect to the NBSR cold neutron guide network (0.064 steradian (sr) and 0.085 sr for 16 × 6 cm × 15 cm and 16 × 6 cm × 20 cm guide entrances (NNS), respectively compared with 0.0428 sr for the 12 cold neutron guides at the NBSR - factors 1.5 and 2.0, respectively), and improved overall cold neutron guide illumination of the NNS CNS (especially with respect to Unit 2). Overall, the gains in usable cold neutron current are about a factor 10 with respect to the existing Unit 2 CNS and about a factor 5 with respect to the future Unit 3 CNS. Potentially higher cold neutron current gains at the guide entrances are possible with a larger CNS diameter (Sec. 2.1.3) and with larger guide entrances.

### 2.1.3. Effect of CNS diameter on CNS brightness

Additional MCNP simulations indicate that moderate increases in the CNS LD<sub>2</sub> vessel diameter at the same axial position may lead to enhanced cold neutron brightness for wavelengths greater than 3 Å, but with diminishing returns as the diameter approaches 40 cm. The results for several CNS diameters are compared with the NBSR Unit 2 and Unit 3 CNS in **Figure 4**. Again, the “usable” divergence restriction  $\mu \geq 0.99875$  was imposed. The corresponding brightness ratios relative to Unit 2 and Unit 3 are shown in Figure 5 and Figure 6, respectively. Note that increasing the vessel diameter without reducing the height is at the expense of increased CNS heat load and LD<sub>2</sub> inventory, so the CNS neutronic performance gain will be weighed against such disadvantages as the design evolves. **Appendix C** shows visuals of the NNS CNS diameters investigated.

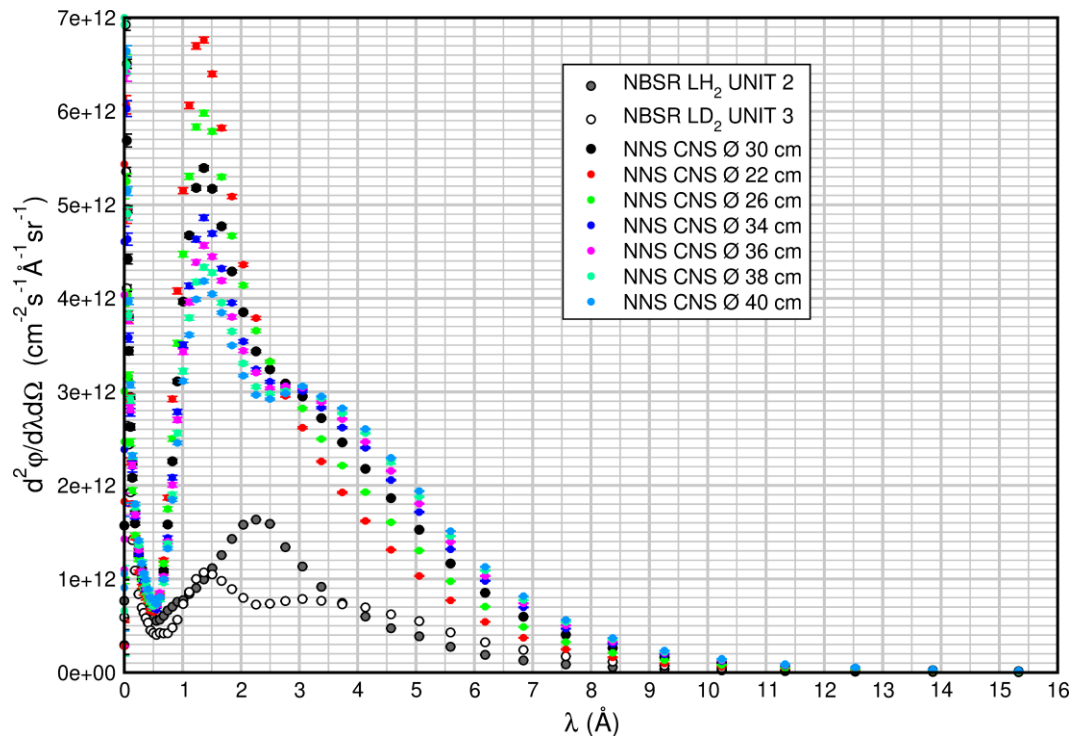


Figure 4. Simulated usable CNS brightness as a function of neutron wavelength for NNS CNS models with various LD<sub>2</sub> vessel diameters indicated in the legend and for the current NBSR Unit 2 LH<sub>2</sub> CNS and the future NBSR Unit 3 LD<sub>2</sub> CNS (see legend). The reference OPAL-like ( $\varnothing$  30 cm) CNS model is represented by solid black circles.

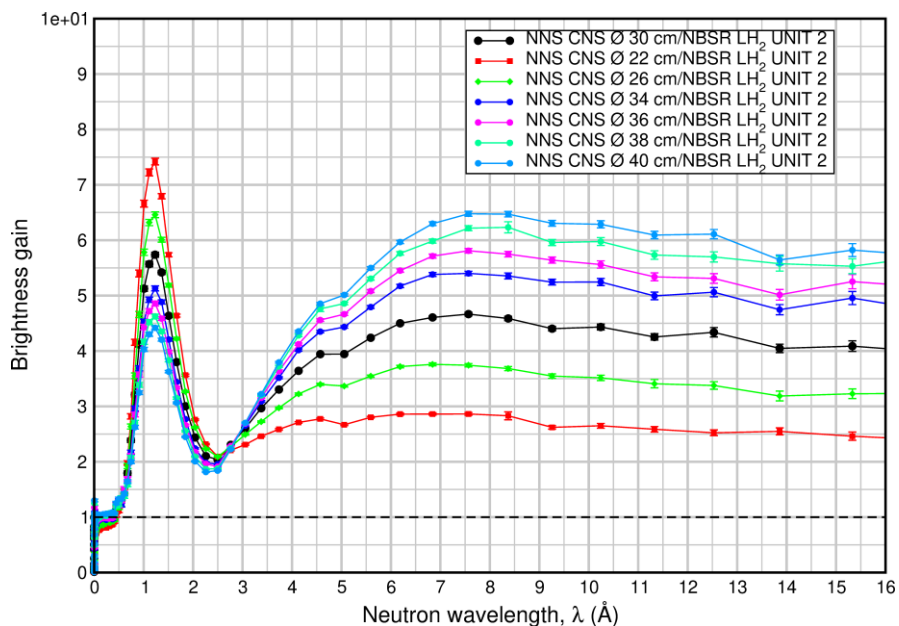


Figure 5. NNS CNS neutron brightness ratios with respect to the present NBSR LH<sub>2</sub> Unit 2 CNS brightness (obtained from the results shown in Figure 4) for the NNS LD<sub>2</sub> vessel diameters indicated in the legend. The reference OPAL-like ( $\varnothing$  30 cm) CNS model is represented by solid black circles.

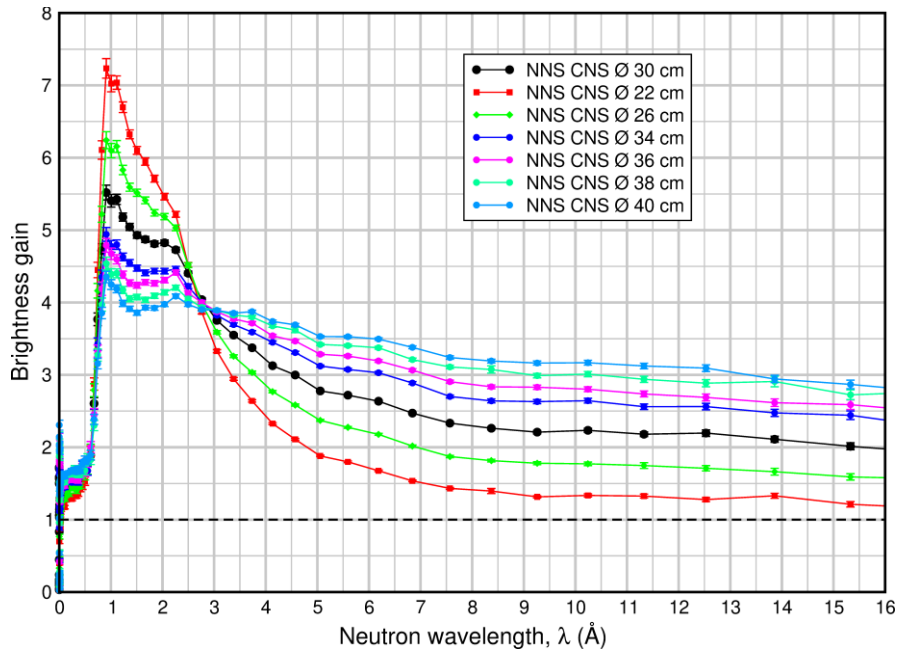
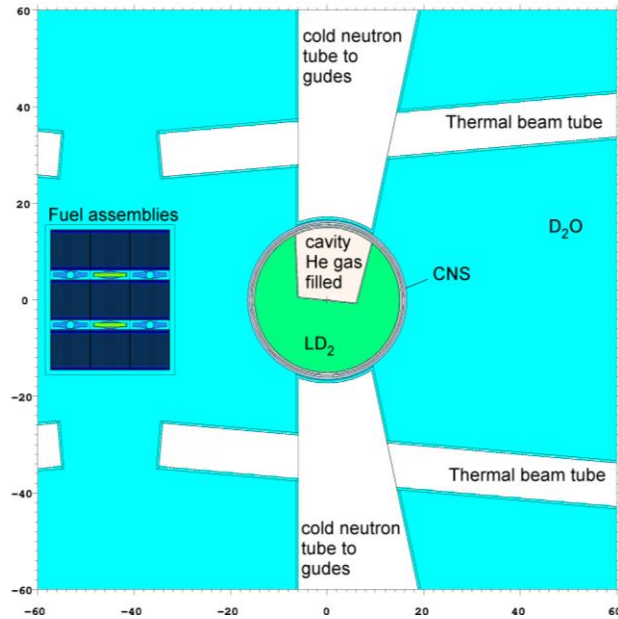


Figure 6. NNS CNS neutron brightness ratios with respect to the future NBSR LD<sub>2</sub> Unit 3 CNS brightness (obtained from the results shown in Figure 4) for the NNS LD<sub>2</sub> vessel diameters indicated in the legend. The reference OPAL-like ( $\varnothing$  30 cm) CNS model is represented by the solid black circles.

#### 2.1.4. Effect of a CNS cavity (re-entrant hole) on the CNS brightness in the beam direction

Introducing a cavity into the CNS may enhance the cold neutron flux in the beam direction [16]. In the OPAL CNS design, this is accomplished by placing a He-filled displacer inside the LD<sub>2</sub> vessel. The current MCNP CNS model cavity is illustrated in plan view through the center of the CNS in Figure 7.



**Figure 7. Plan view through the center of the current MCNP model showing the CNS with one cavity.**

Preliminary studies with the CNS axis centered at the (31.82 cm, 31.82 cm) location showed a cold neutron enhancement on the cavity side. Simulations with the latest model (with the CNS axis centered at the ( $\pm 45$  cm, 0)) show similar results (c.f. light blue and dark green curves in Figure 2) with the corresponding wavelength-dependent cold neutron gains shown in Figure 8. However, introducing a more symmetrical, shallower, or reshaped dual-cavity arrangement could significantly complicate the internal CNS structure, as noted by Williams in his review of the OPAL CNS upgrade project (Appendix A). Nonetheless, further optimization of the cavity configuration of the NNS CNS will be explored following the pre-conceptual design phase, including consideration of the heat load impact.

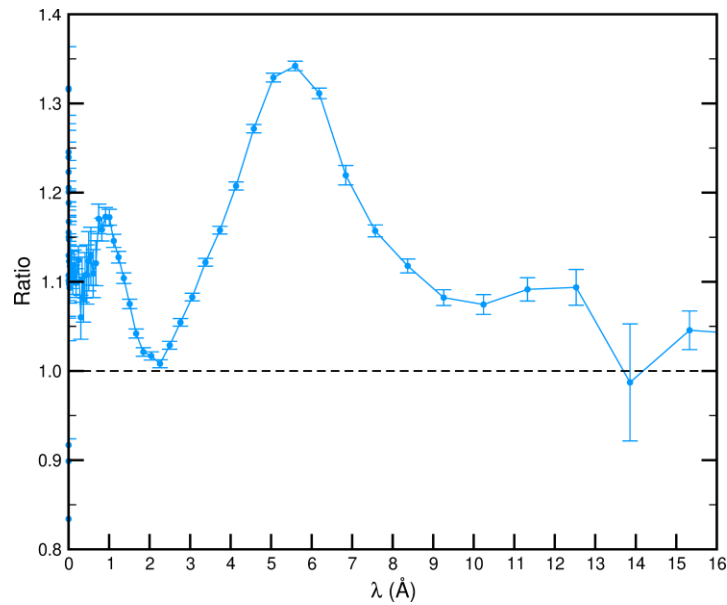


Figure 8. Simulated neutron brightness gain from viewing the cavity side of the CNS in the current model as opposed to the non-cavity side (ratio of light blue to dark green curves in Figure 2).

## 2.2. CNS size and neutron guide illumination

Irrespective of the size and type of cold moderator needed to obtain high cold neutron spectral gains, the CNS cross-sectional area, together with the cold neutron guide design and guide entrance separation, also determine the neutron guide illumination, as illustrated schematically in Figure 9.

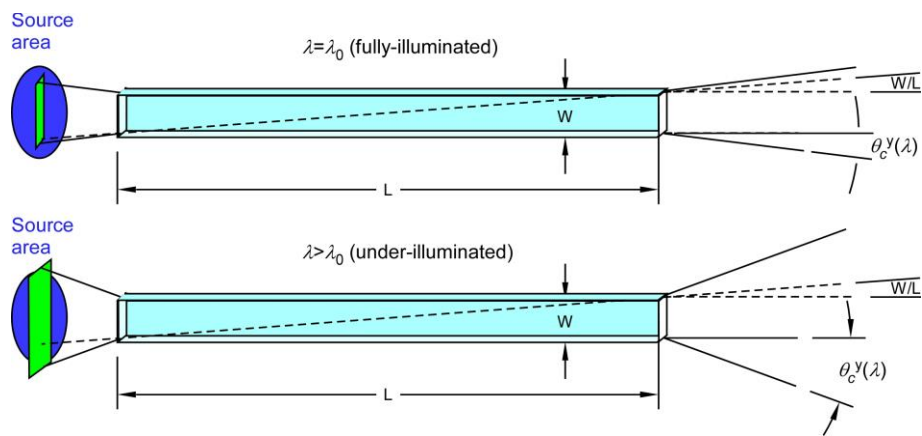


Figure 9. A schematic representation of full-illumination (top) and under-illumination (bottom) of an ideal, long, straight neutron guide. “Long” in this context is for wavelengths satisfying  $W/L < \theta_c$ .

Figure 10 illustrates illumination by plotting the origins of successfully transmitted neutrons projected onto the source cross-section. The figure shows, for several neutron wavelengths, the neutron origins projected onto the cross-section of a vertical CNS LD<sub>2</sub> vessel cylinder of diameter 297 mm and height 305 mm for the challenging example of a tall, high- $m$  guide (guide #4 of group 3 in Ref. [31]). This guide has both a large cross-section (6 cm (width) × 20 cm

(height)) and a large  $m$  ( $m=3.9$ ) supermirror on the bend of the curved section. The top and bottom reflecting surfaces have  $m = 3$ . The guide entrance is assumed to be 1.5 m distant from the CNS center. The reduced point density at the extremities of each patch reveals greater reflection losses for more divergent neutrons that require increased numbers of contacts with the reflecting surfaces, on average, for transmission. The horizontal shift for the shortest wavelengths is an artifact of the initial curvature of the guide. The results show full illumination up to about  $\lambda = 0.8$  nm. Therefore, the model CNS height is likely ample even for taller, high- $m$  guides, and further increasing the vessel diameter serves only to increase the cold neutron brightness (see Sec. 2.1.2). Tall guides are favorable for extracting multiple beams from multiple levels or when a large initial beam height can be focused onto the sample.

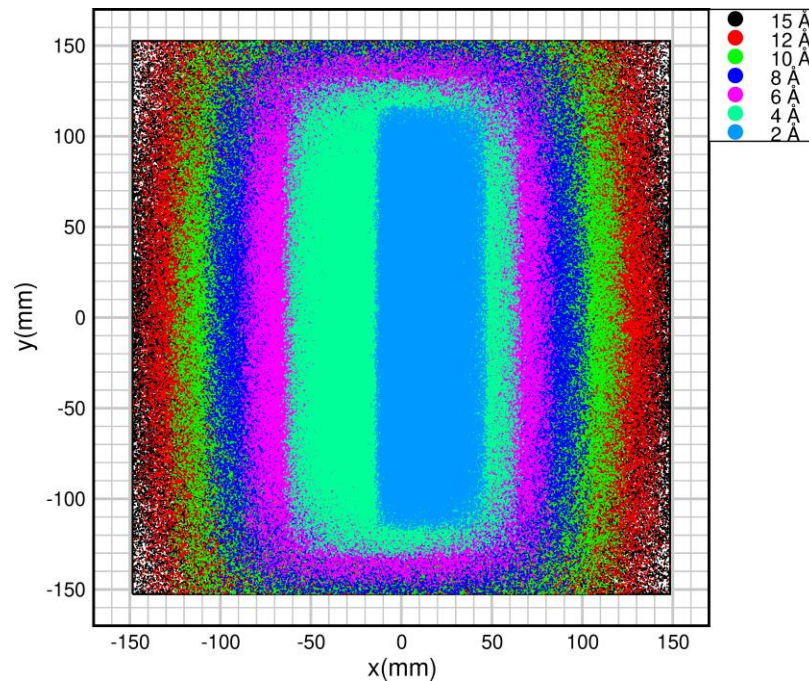


Figure 10. Simulated origins of neutrons on a rectangular cross-section source that are transmitted to the exit of group #3, guide #4 described in Ref. [31] for several neutron wavelengths.

### 2.2.1. Optimization of CNS height

The CNS height should be reasonably minimized for several reasons, including reducing  $LD_2$  inventory and the CNS heat load. Consequently, it should be no taller than necessary to produce optimal or near-optimal transmission of neutrons that can be used by the instruments. The diminishing returns from the top and bottom of the CNS are due to several considerations:

- (i) The top and bottom neutrons tend to contribute more divergent neutrons that cannot reach the sample and cause an unwanted background.
- (ii) The larger reflection angles of more divergent neutrons originating from the top and bottom of the CNS tend to suffer increased reflection losses due to reduced high momentum transfer reflectivity and an increased number of contacts with the

reflecting surface of the guide that multiply such losses. Consequently, on average, these neutrons are transmitted less efficiently than less divergent neutrons.

- (iii) The vertical cold neutron flux profile at the CNS usually offers reduced brightness at the top and bottom compared to the center.

### 2.3. LD<sub>2</sub> CNS size and nuclear heat load

A practical constraint on the volume of the CNS (other than deuterium inventory) remains the ability to remove sufficient heat from the CNS cryogenic circuit. Replacement of the NBSR LH<sub>2</sub> (Unit 2) CNS [22] with the LD<sub>2</sub> (Unit 3) CNS [21] required a heat load limitation of about 4 kW due to the cooling capacity limitation of the helium refrigerator. The use of a single-phase thermosyphon for the OPAL LD<sub>2</sub> source limited the maximum heat load to about 5 kW [28] [32], and at the RA-10 reactor, the limitation was also about 5 kW [20], but this is not a technical limitation. For example, the refrigerator for the European Spallation Source (ESS) has a capacity of about 30 kW [33]. This was also the anticipated heat load for the ANS project LD<sub>2</sub> cold source [34].

MCNP simulations of nuclear heat load in the cryogenically-cooled CNS elements (within the insulation vacuum) were performed to assess contributions due to:

- (i) Gamma-ray heating
- (ii) Saturation-level <sup>28</sup>Al β heating, and
- (iii) Neutron heating

Simulations were performed for the NNS model CNS vessel diameters given in Sec. 2.1.3 and shown in **Appendix C**. The results are summarized in **Table 6** and Figure 11. The non-nuclear component of the heat load (thermal radiation and heat introduced by conduction and convection) was not estimated here but, based on results for the OPAL CNS at 20 MW reactor power [32], would likely add about 10% to the totals shown in Table 6 (about 400 W for OPAL).

**Table 6. Summary of total heating contributions due to various radiation components and total minimum cryogenic heat loads for NNS CNS as a function of CNS diameter. These values do not include the non-nuclear heat, which is estimated to be about 10% in addition.**

Component	Total Nuclear Heating (W)						
	∅ 22 cm	∅ 26 cm	∅ 30 cm	∅ 34 cm	∅ 36 cm	∅ 38 cm	∅ 40 cm
<i>Gamma (γ)</i>	1347	1782	2220	2857	3175	3512	3873
Saturation <sup>28</sup> Al β	1142	1439	1710	2084	2252	2423	2591
Neutron	219	358	583	885	1091	1340	1630
<b>TOTAL</b>	<b>2708</b>	<b>3579</b>	<b>4513</b>	<b>5826</b>	<b>6518</b>	<b>7275</b>	<b>8094</b>

It is observed that the increase in nuclear heat load (and of the heating due to individual radiation components) increases approximately quadratically with the CNS vessel diameter (roughly proportional to the CNS volume). This is illustrated in Figure 11. If the CNS diameter were increased to about 36 cm to gain cold neutron brightness (Figure 5), the nuclear heat load per CNS would increase to about 6.5 kW, requiring at least 15 kW total cooling capacity.

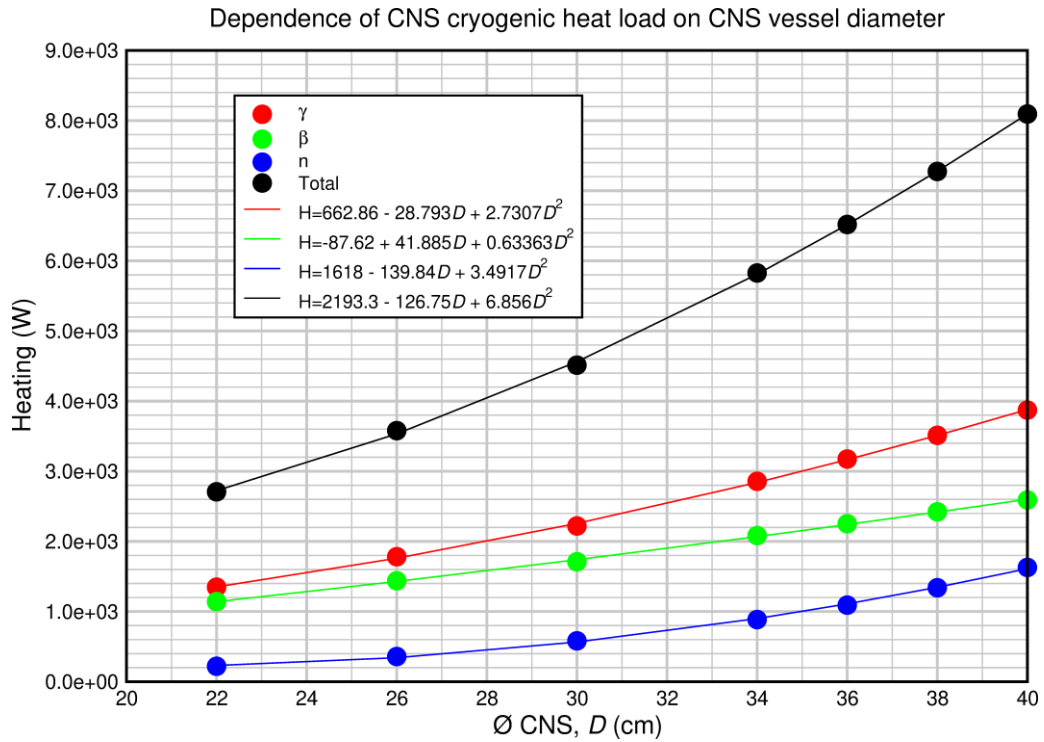


**Figure 11. Dependence of the CNS cryogenic system radiation heat load vs. model CNS vessel diameter. The Al-6061 layer thicknesses for each model are assumed unchanged from the current (Ø 30 cm) model values.**



### 3. Nuclear heating of aluminum-alloy-substrate in-pile cold neutron guides

A preliminary estimate of nuclear heating in aluminum-alloy-substrate in-pile cold neutron guides was performed. The result (Figure 12) includes heating from gamma rays, neutrons, and saturation-level  $^{28}\text{Al}$   $\beta$  particles produced from neutron absorption in the Al substrate, but no non-nuclear component was included. A conservative absolute upper-limit temperature estimate is obtained by assuming heat loss only by radiation from the "exposed" surfaces to a sink at 25 C. The emissivity of the aluminum alloy is very dependent on surface finish and treatment. Assuming an emissivity  $\varepsilon = 0.1$  for Al6061-T6 at room temperature yields a maximum equilibrium temperature  $T = 193$  C for the first element and 232 C for the second element. If, however,  $\varepsilon = 0.2$ , the same calculation yields 134 C and 164 C, respectively. Reactively sputtered Ni-Ti supermirrors are stable up to about 260 C. Accounting for the high thermal conductivity of the Al6061 substrate and forced convection cooling from a helium flow, we anticipate guide temperatures well within tolerance for a 1.5 m CNS-guide separation.

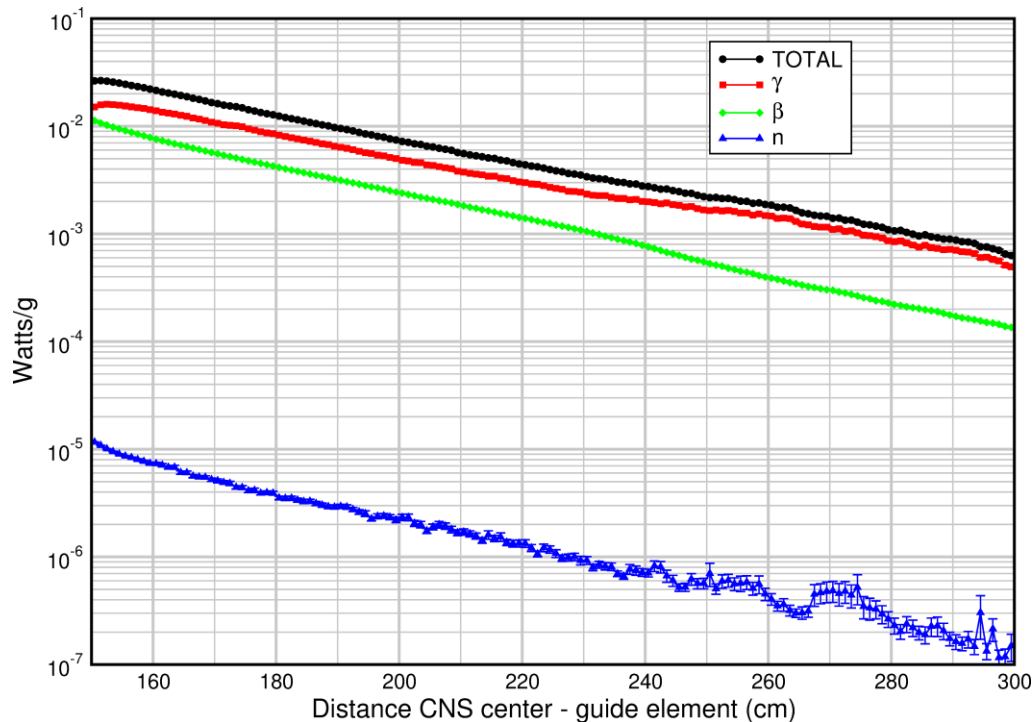


Figure 12. Estimated nuclear heating per unit mass ( $\text{Wg}^{-1}$ ) for Al-substrate in-pile cold neutron guides with entrances 1.5 m from the center of the CNS and 20 MW reactor power. The red curve is gamma heating, the green curve is saturation-level  $^{28}\text{Al}$ -decay  $\beta$ , the blue curve is neutron, and the black curve is the total heating.

## 4. Thermal beams

The thermal neutron beams are envisioned approximately perpendicular to the cold neutron beams, tangential to the sides of the core without cold neutron sources. It may be possible to intersect the thermal and cold neutron beam tubes, as shown in Figure 13, provided there are no structures at the intersections. Alternatively, the beams may be extracted at different heights but close to the thermal neutron flux peak. (The lines visible at the beam intersections in Figure 13 are model cell boundaries, not physical ones).

### 4.1. Thermal brightness and dependence on beam tube position

Preliminary simulations of the thermal neutron brightness along a thermal beam tube of sufficient cross-section to accommodate a 6 cm × 20 cm internal dimension thermal neutron guide (Figure 13) are shown in Figure 14. The results are compared with analogous simulations for the present NIST research reactor (NBSR) thermal tube BT-6 at the shield exit. A polar angle restriction along the beam tube axis of 2.9° ( $\mu = \cos \theta > 0.99875$ ) was imposed to assess the brightness within the solid angular range imposed by the beam tube collimation more accurately. The BT-6 simulations have a polar angle restriction of about 3° (wintergreen-colored curves). The results indicate a factor 2 increase in thermal brightness with respect to the NBSR at 20 MW. Preliminary results for parallel displacements of the thermal tube indicate that displacing the tube towards the fuel only increases the fast neutron flux with a negligible increase of the thermal flux, whereas moving the tube away from the fuel results in a drop in the thermal flux. Thus, the position shown in Figure 13 appears close to optimum. Nonetheless, the position and thimble positioning will be refined once the core design is more advanced. The thermal beam tube exit of the biological shield (2.5 m thick) of the current MCNP model is approximately 3.37 m from the tally position (4.87 m from the tube entrance).

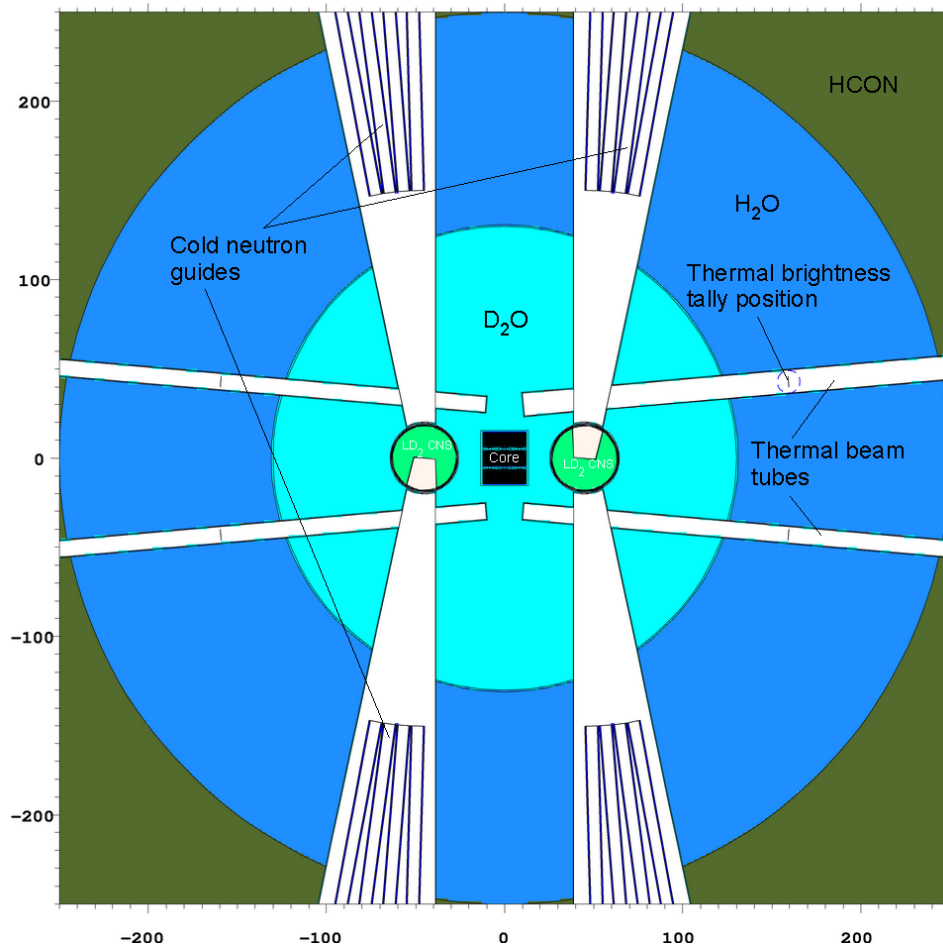


Figure 13. Plan view through the fuel center of the reactor core. The thermal neutron brightness spectrum was tallied at the position indicated by the blue circle on the larger thermal tube to the upper right.

Thermal brightness comparison NBSR - NNS

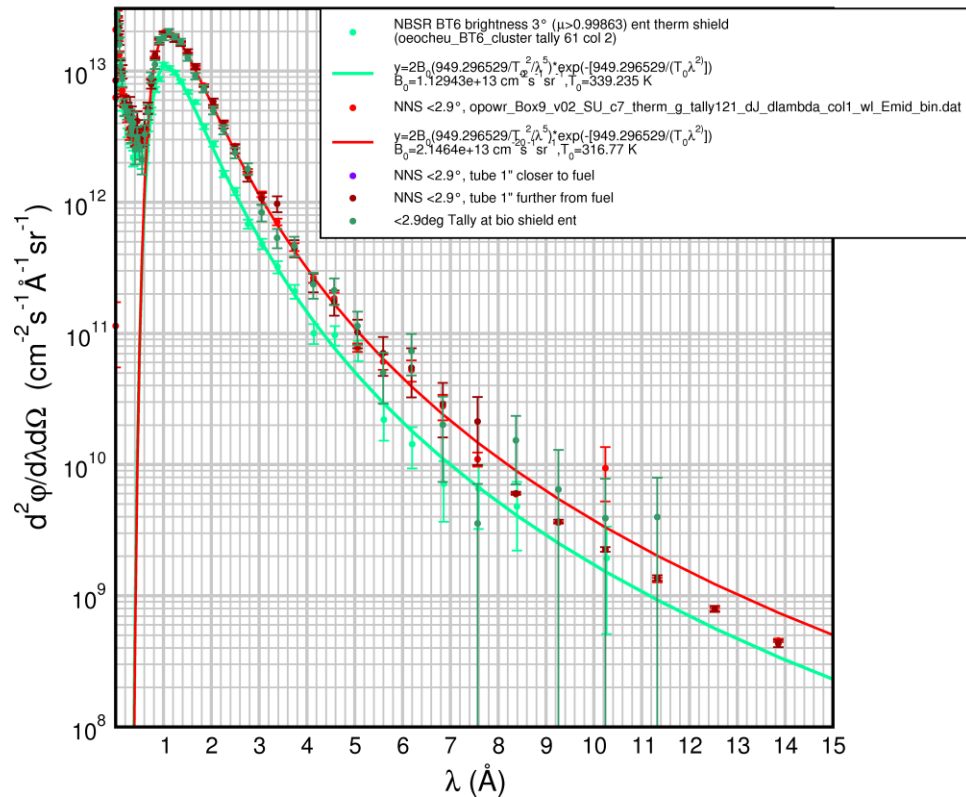


Figure 14. Simulated thermal neutron brightness vs. neutron wavelength for the NNS (red points) at the position indicated by the blue dashed circle in Figure 13. The wintergreen colored points are similar simulations for the NBSR BT6 beam at the shield exit. The solid curves are Maxwellian fits. A fitted effective temperature of 317 K for the NNS indicates that the contributing spectrum is well-thermalized.

#### 4.2. Performance of thermal neutron guides

Thermal neutron guides may facilitate instrument layout by enabling some to be placed further from the biological shield in lower background radiation with less penalty for the increased distance - particularly those instruments using longer wavelengths in the thermal range. To be effective, the solid angle for direct (unreflected) neutron transmission through a neutron guide should not be large compared with the solid angle range that can be reflected from the guide. Therefore, thermal neutron guides usually have high- $m$  supermirror coatings to compensate for the shorter wavelength thermal neutrons' lower critical angles (maximum reflection angles). Furthermore, thermal neutron instruments sometimes use large beams. In such cases, the idealized 1-dimensional neutron guide transmission is often in a regime where the idealized gain factor is  $1 + \theta_c^2 / \psi_0^2$ , where  $\theta_c$  is the critical angle, and  $\psi_0$  is the guide width:length ratio [35]. Therefore, the critical angle for any dimension should probably be at least 30% of the width (or height): length ( $W/L$ ) ratio of the guide to be worth considering at all. Consequently, thermal neutron guides benefit such instruments only if they are placed sufficiently far from the source or if the cross-section is subdivided by multiple neutron reflecting surfaces (so-called channeled devices) in order to reduce  $W/L$ .

The following example assumes the NNS thermal source brightness represented by the red curve in Figure 14:

The mean neutron flux is simulated on a 6 cm (w) × 20 cm (h) target area either:

- (i) Through an empty 15 cm (w) × 25 cm (h) cross-section biological shield penetration  
or
- (ii) With an intervening 6 cm (w) × 20 cm (h) thermal neutron guide whose entrance starts at the entrance to the biological shield (see Figure 15).

In all cases, simulations were performed for a 6 cm (w) × 20 cm (h) target area at several distances,  $d$ , from the exit of the 2.5 m-thick biological shield. The intensities at each position are compared in the central column of **Figure 16** (i) for the bare tube (black curves) and (ii) at the guide exits (red curves). The corresponding guide gains as a function of wavelength are shown in the right-hand column of **Figure 16**. The results show that both the threshold wavelengths for potential flux gains from a thermal neutron guide over a bare tube reduce as the target position moves away from the source and the importance of the reflected neutrons in the guide increases. Also, the absolute gain factors above the threshold wavelengths increase as the target position moves away from the core. For instruments close to the reactor face, there is no use for a neutron guide for thermal wavelengths, and the guide area restriction reduces the flux for wavelengths less than 0.5 nm (5 Å). However, for  $d \geq 8$  m, the guide may provide a valuable gain for thermal instruments using greater than (say) 0.15 nm (1.5 Å) neutrons. While the guide may not compensate for the intensity gain of placing the instrument closer to the source, it may facilitate additional thermal instrument placement. Specific optimization of thermal guide design and entrance-exit placement will be performed after the pre-conceptual design phase.

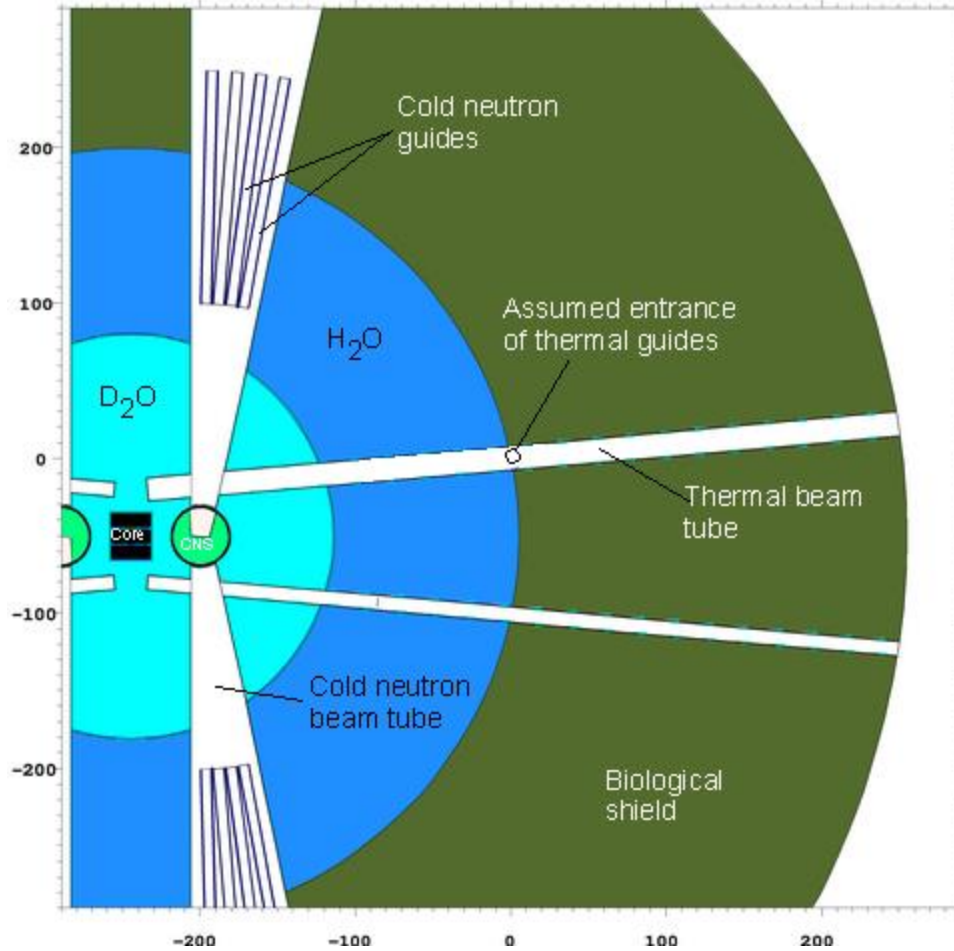


Figure 15. Plan view showing thermal beam tubes. The beam tube penetrates the biological shield (dark green) and is large enough to accommodate a 6 cm(w) × 20 cm (h) thermal neutron guide. The 6 cm × 20 cm thermal guides are assumed to start at the entrance to the biological shield (blue dashed circle).

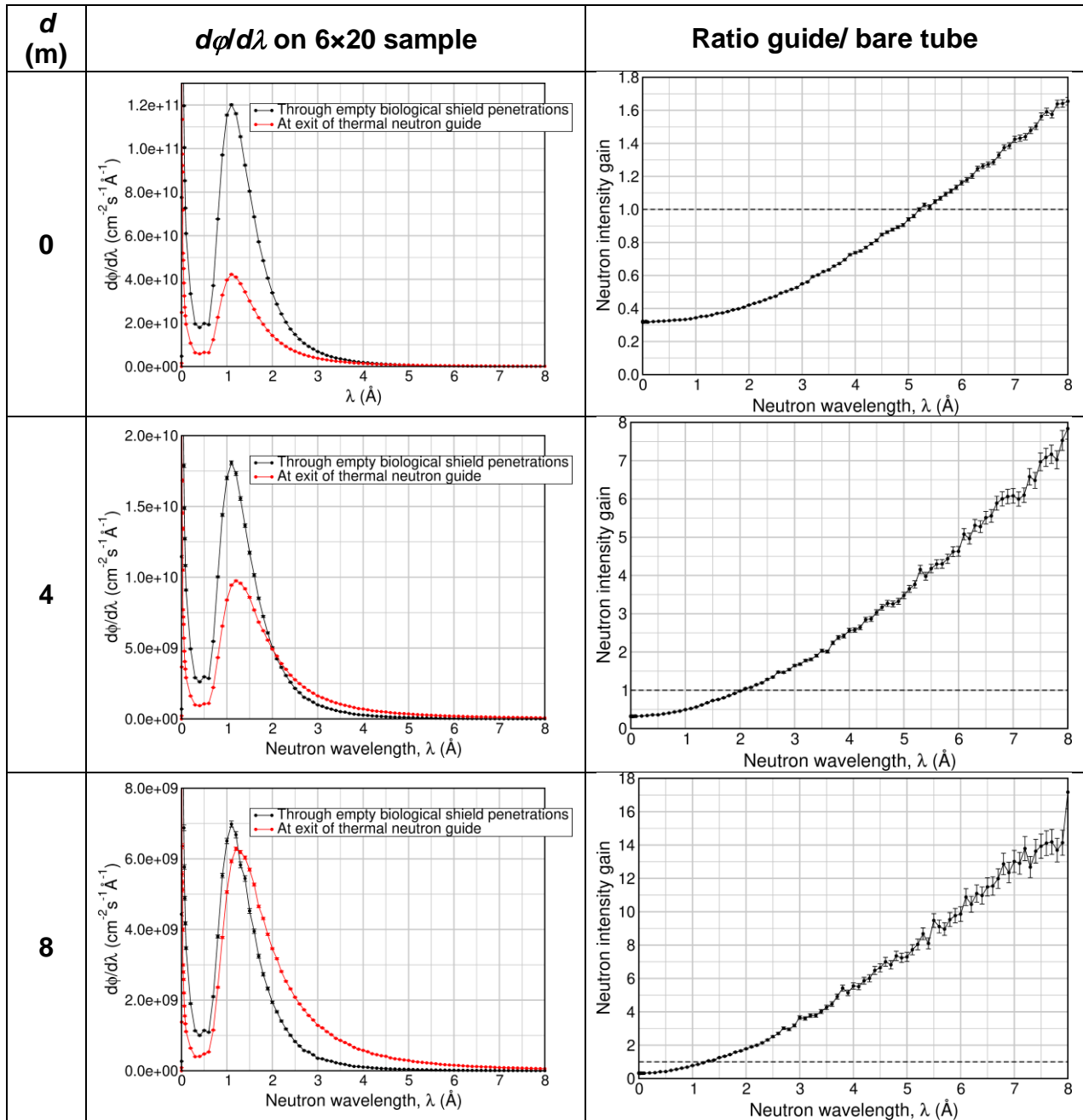


Figure 16. Center column: Simulated thermal neutron intensities (flux per unit wavelength) as a function of neutron wavelength on a 6 cm(w) × 20 cm (h) target at a distance  $d$  (m) from the exit of the biological shield. Black curves: Through the empty 15 cm(w) × 25 cm(h) biological shield penetration. Red curves: At the exit of a 6cm × 20cm thermal neutron guide starting at the entrance to the biological shield. The corresponding guide gains (ratio of red to black curves) are shown in the right-hand column.

## References

- [1] Şahin D, Çelikten OŞ, Cook JC, Weiss AG, Newton TH, Diamond D, Majkrzak CF, King HE, Shen J, Gurgun A, Nahmani E, Baroukh IR, Cheng, L-Y (2022) NIST Neutron Source Preconceptual Design. *RERTR 2022 – 42ND INTERNATIONAL MEETING ON REDUCED ENRICHMENT FOR RESEARCH AND TEST REACTORS* (IAEA, Vienna). Available at [https://www.rertr.anl.gov/RERTR42/pdfs/S7-P6\\_Sahin\\_paper.pdf](https://www.rertr.anl.gov/RERTR42/pdfs/S7-P6_Sahin_paper.pdf)
- [2] Sahin D, Celikten O, Cook JC, Weiss A, Newton T, Diamond D, Majkrzak C, King H, Shen J, Gurgun A, Cheng L-Y, Kohut P, Lu C, Varuttamaseni A (2023) Pre-Conceptual Design of the NIST Neutron Source. (The European Research Reactor Conference, Antwerp, BE). Available at [https://tsapps.nist.gov/publication/get\\_pdf.cfm?pub\\_id=936488](https://tsapps.nist.gov/publication/get_pdf.cfm?pub_id=936488)
- [3] Cook JC, King HE, Majkrzak CF, Sahin D, Shen JS, Celikten OS, Diamond D, Williams RE, Newton TH (2022) Proposed NIST Neutron Source User Facility. *Transactions of the American Nuclear Society* (American Nuclear Society, Phoenix, AZ), pp 608–611. <https://doi.org/doi.org/10.13182/T127-39654>
- [4] Cook JC, King HE, Majkrzak CF, Şahin D, Diamond D, Shen JS, Celikten OS, Williams RE, Newton TH (2022) Neutron Delivery Systems Design of the Proposed NIST Neutron Source. *Transactions of the American Nuclear Society* (American Nuclear Society, Phoenix, AZ), pp 1020–1022. <https://doi.org/doi.org/10.13182/T127-39643>
- [5] Jeremy C. Cook, Hubert E. King, Charles F. Majkrzak, Dan A. Neumann (2024) Pre-conceptual Design Activities of the NIST Neutron Source: Preliminary Layout of Cold and Thermal Neutron Instruments. <https://doi.org/10.6028/NIST.TN.2280>
- [6] Butterworth I, Egelstaff PA, London H, Webb FJ (1957) The production of intense cold neutron beams. *The Philosophical Magazine: A Journal of Theoretical Experimental and Applied Physics* 2(19):917–927. <https://doi.org/10.1080/14786435708242730>
- [7] Webb FJ (1963) Cold neutron sources. *Journal of Nuclear Energy Parts A/B Reactor Science and Technology* 17(4):187–215. [https://doi.org/10.1016/0368-3230\(63\)90021-1](https://doi.org/10.1016/0368-3230(63)90021-1)
- [8] P. Ageron, Ph. De Beaucourt, H. d. Harig, A. Lacaze, M. Livolant (1969) Experimental and Theoretical Study of Cold Neutron Sources of Liquid Hydrogen and Liquid Deuterium. *Cryogenics* 9(1):42–50. [https://doi.org/10.1016/0011-2275\(69\)90257-4](https://doi.org/10.1016/0011-2275(69)90257-4)
- [9] Kai T, Harada M, Teshigawara M, Watanabe N, Ikeda Y (2004) Coupled hydrogen moderator optimization with ortho/para hydrogen ratio. *Nuclear Instruments and Methods in Physics Research Section A: Accelerators, Spectrometers, Detectors and Associated Equipment* 523(3):398–414. <https://doi.org/10.1016/j.nima.2003.11.427>
- [10] Batkov K, Takibayev A, Zanini L, Mezei F (2013) Unperturbed moderator brightness in pulsed neutron sources. *Nuclear Instruments and Methods in Physics Research Section A:*



- Accelerators, Spectrometers, Detectors and Associated Equipment* 729:500–505. <https://doi.org/10.1016/j.nima.2013.07.031>
- [11] Magán M, Sordo F, Zanini L, Terrón S, Ghiglini A, Martínez F, de Vicente JP, Vivanco R, Perlado JM, Bermejo FJ, Mezei F, Muhrer G (2013) Neutronic analysis of the bi-spectral moderator such as that proposed for ESS. *Nuclear Instruments and Methods in Physics Research Section A: Accelerators, Spectrometers, Detectors and Associated Equipment* 729:417–425. <https://doi.org/10.1016/j.nima.2013.07.011>
- [12] Ooi M, Ino T, Muhrer G, Pitcher EJ, Russell GJ, Ferguson PD, Iverson EB, Freeman D, Kiyonagi Y (2006) Measurements of the change of neutronic performance of a hydrogen moderator at Manuel Lujan Neutron Scattering Center due to conversion from ortho- to para-hydrogen state. *Nuclear Instruments and Methods in Physics Research Section A: Accelerators, Spectrometers, Detectors and Associated Equipment* 566(2):699–705. <https://doi.org/10.1016/j.nima.2006.06.073>
- [13] Grammer KB, Alarcon R, Barrón-Palos L, Blyth D, Bowman JD, Calarco J, Crawford C, Craycraft K, Evans D, Fomin N, Fry J, Gericke M, Gillis RC, Greene GL, Hamblen J, Hayes C, Kucuker S, Mahurin R, Maldonado-Velázquez M, Martin E, McCrea M, Mueller PE, Musgrave M, Nann H, Penttilä SI, Snow WM, Tang Z, Wilburn WS (2015) Measurement of the scattering cross section of slow neutrons on liquid parahydrogen from neutron transmission. *Physical Review B* 91(18):180301. <https://doi.org/10.1103/PhysRevB.91.180301>
- [14] Fessler TE, Blue JW (1965) Radiation-Induced Conversion of Liquid Hydrogen. *Physical Review Letters* 14(20):811–812. <https://doi.org/10.1103/PhysRevLett.14.811>
- [15] Cook JC, Barker JG, Rowe JM, Williams RE, Gagnon C, Lindstrom RM, Ibberson RM, Neumann DA (2015) Experimental characterization of the Advanced Liquid Hydrogen Cold Neutron Source spectrum of the NBSR reactor at the NIST Center for Neutron Research. *Nuclear Instruments and Methods in Physics Research Section A: Accelerators, Spectrometers, Detectors and Associated Equipment* 792:15–27. <https://doi.org/10.1016/j.nima.2015.04.037>
- [16] Ageron P (1989) Cold neutron sources at ILL. *Nuclear Instruments and Methods in Physics Research Section A: Accelerators, Spectrometers, Detectors and Associated Equipment* 284(1):197–199. [https://doi.org/10.1016/0168-9002\(89\)90281-7](https://doi.org/10.1016/0168-9002(89)90281-7)
- [17] Farhi E, Calzavara Y Discussion about published brightness evaluations of the ILL.
- [18] Gaubatz W, Gobrecht K (2000) The FRM-II cold neutron source. *Physica B: Condensed Matter* 276–278:104–105. [https://doi.org/10.1016/S0921-4526\(99\)01260-0](https://doi.org/10.1016/S0921-4526(99)01260-0)

- [19] Kennedy SJ (2006) Construction of the neutron beam facility at Australia's OPAL research reactor. *Physica B: Condensed Matter* 385–386:949–954. <https://doi.org/10.1016/j.physb.2006.05.280>
- [20] Márquez A, Sánchez F (2014) Neutron Cold Source Optimization for RA-10 reactor. *Proceedings of the 16th Meeting of the International Group On Research Reactors* (Bariloche, Argentina). Available at <https://www.igorr.com/Documents/2014-BARILOCHE/arielMarquez.doc>
- [21] Williams RE, Middleton M, Kopetka P, Rowe JM, Brand PC (2013) A Liquid Deuterium Cold Neutron Source for the NIST Research Reactor - Conceptual Design. *Proceedings of the 15th Meeting of the International Group on Research Reactors* (Daejeon, South Korea). Available at [https://www.igorr.com/Documents/2013-DAEJEON/07\\_1003.pdf](https://www.igorr.com/Documents/2013-DAEJEON/07_1003.pdf)
- [22] Kopetka P, Williams RE, Rowe JM (2006) NIST liquid hydrogen cold source. (National Institute of Standards and Technology, Gaithersburg, MD), NIST IR 7352, 0 Ed., p NIST IR 7352. <https://doi.org/10.6028/NIST.IR.7352>
- [23] McFarlane, Robert E. Cold-Moderator Scattering Kernel Methods., la-ur-98-0655.pdf. Available at [https://mcnp.lanl.gov/pdf\\_files/la-ur-98-0655.pdf](https://mcnp.lanl.gov/pdf_files/la-ur-98-0655.pdf)
- [24] Conlin JL (2017) Listing of Available ACE Data Tables. (Los Alamos National Lab. (LANL), Los Alamos, NM (United States)), LA-UR-17-20709, p 503. Available at <https://permlink.lanl.gov/object/tr?what=info:lanl-repo/lareport/LA-UR-17-20709>
- [25] Atchison F, Beaud P, Bryś T, Daum M, Fierlinger P, Henneck R, Hofmann T, Kirch K, Kühne G, Knopp G, Pichlmaier A, Serebrov A, Spitzer H, Wambach J, Wimmer J, Wokaun A, Bodek K, Geltenbort P, Giersch M, Zmeskal J, Mishima K (2003) Ortho-para equilibrium in a liquid D<sub>2</sub> neutron moderator under irradiation. *Phys Rev B* 68(9):094114. <https://doi.org/10.1103/PhysRevB.68.094114>
- [26] Masriera N, Lovotti O, Lecot C, Hergenreder D, Serebrov A, Mityukhlyev V, Zakharov A (2003) Development of the RRR Cold Neutron Source Facility. *Proceedings of the 9th Meeting of the International Group on Research Reactors* (Sydney Australia).
- [27] Lu W (2009) Early Operational Experience of the Cold Neutron Source on OPAL Reactor. Available at </web/20230510170411/https://www.igorr.com/Documents/2009-BEIJING/Weijian%20Lu-Presentation.pdf>
- [28] Pavlou T, Ho M, Yeoh GH, Lu W (2016) Thermal-hydraulic modelling of the Cold Neutron Source thermosiphon system. *Annals of Nuclear Energy* 90:135–147. <https://doi.org/10.1016/j.anucene.2015.11.034>
- [29] S. Kim (2007) Cold Neutron Source at OPAL Reactor, ANSTO. Available at </web/20230510175404/https://www.engineersaustralia.org.au/sites/default/files/resource-files/2017-01/Cold%20Neutron.pdf>

- [30] Liouville J (1838) Note sur la Théorie de la Variation des constantes arbitraires. *Journal de Mathématiques Pures et Appliquées* 1e série, 3. Available at [http://www.numdam.org/item/JMPA\\_1838\\_1\\_3\\_\\_342\\_0/](http://www.numdam.org/item/JMPA_1838_1_3__342_0/)
- [31] Cook JC, Majkrzak CF, King HE, Neumann DA (2023) Pre-conceptual Design Activities of the NIST Neutron Source: Preliminary Layout of Cold & Thermal Neutron Instruments. *NIST Technical Note* XX:XX–XX.
- [32] Lu W, Thiering R (2009) The OPAL Cold Neutron Source Heat Load Measurements. *Proceedings of 12th Meeting of the International Group On Research Reactors* (Beijing, China). Available at <https://www.igorr.com/Documents/2009-BEIJING/Weijian%20Lu.pdf>
- [33] Beßler Y, Natour G (2022) Cryogenic hydrogen Moderator infrastructure at ESS. *Journal of Neutron Research* 24(2):239–246. <https://doi.org/10.3233/JNR-220033>
- [34] Lucas AT (1995) The Advanced Neutron Source liquid deuterium cold source., ORNL/TM--13058, 211649, p ORNL/TM--13058, 211649. <https://doi.org/10.2172/211649>
- [35] Carpenter JM, Mildner DFR (1982) Neutron guide tube gain for a remote finite source. *Nuclear Instruments and Methods in Physics Research* 196(2):341–348. [https://doi.org/10.1016/0029-554X\(82\)90097-0](https://doi.org/10.1016/0029-554X(82)90097-0)

## Appendix A - Review of Proposed Mark II LD<sub>2</sub> CNS for OPAL: by Robert E. Williams

### SUMMARY

The existing liquid deuterium cold neutron source in OPAL, operating since 2006, has a finite lifetime dictated by the cumulative neutron fluence and the behavior of the material used in its fabrication. The source must be replaced in 2019. This requirement opens the possibility of modifying the design if it can be shown that the Mark II CNS can increase the cold neutron performance. I have been asked to review the computational tools and procedures used to evaluate proposals for Mark II design options. My conclusions and recommendations are presented in this report, along with a review of the major findings in support of the installation of a taller but otherwise unchanged LD<sub>2</sub> moderator vessel. ***I recommend that ANSTO proceed with the detailed design and fabrication of the Mark II In-pile Assembly and continue planning for its installation in 2019.***

### Background:

The OPAL cold source is unique among LD<sub>2</sub> sources in that it operates with a single-phase thermosiphon and it features direct cooling of the moderator vessel as shown in Figure A-1. The main components of the in-pile assembly are: (1) a counter-flow heat exchanger, (2) the LD<sub>2</sub> supply line, (3) the double-walled moderator vessel, and (4) the return line. Natural circulation of the liquid deuterium is driven by the density difference between the warm LD<sub>2</sub> rising in the return line and the colder stream of liquid descending from the heat exchanger displacing it. Both the moderator vessel and the heat exchanger are cooled by helium refrigerant which enters at two points. In the normal operating (NO) mode, the He inlet temperature is about 20 K, which is sufficient to maintain the deuterium as a subcooled liquid. The NO mode requires that both of the He compressors are operating properly.

A great advantage of direct cooling is that in the event of a compressor failure, the second compressor can deliver sufficient flow to protect the in-pile assembly from overheating even with OPAL at full power. In this standby operating (SO) mode, the facility has been able to continue its primary mission of supplying the nation with much-needed medical radioisotopes. Unfortunately, the neutron scattering program of the Bragg Institute is severely diminished by the lack of cold neutrons in the SO mode. Operation in the SO mode has allowed careful measurements of the nuclear heat load in the absence of the LD<sub>2</sub> to compare with measurements in the NO mode, providing benchmarks for computational models.

Additional benchmarks can be made using a series of time-of-flight (TOF) cold neutron flux spectrum measurements, beginning with those performed during the commissioning of the reactor to confirm that the CNS was able to meet performance specifications set forth in the original contract with INVAP. More recent TOF measurements were made at CG-1 in 2013. Two cold neutron beam ports view the CNS as shown in Figure A-2. A helium-filled displacer, serving as a reentrant hole, was introduced in the original CNS design to enhance the cold neutron flux to CG 1-3 serving several instruments in the Guide Hall. Details of the displacer are shown in Figure A-3; it is part of the He refrigerant loop.

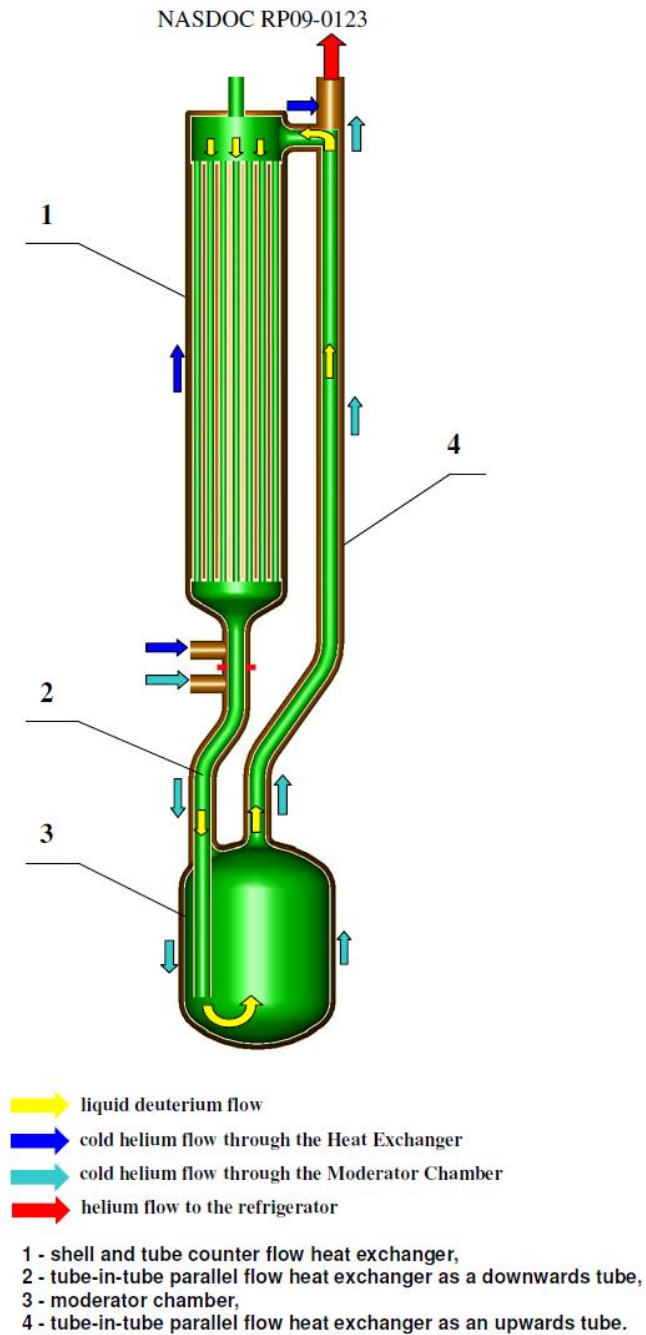
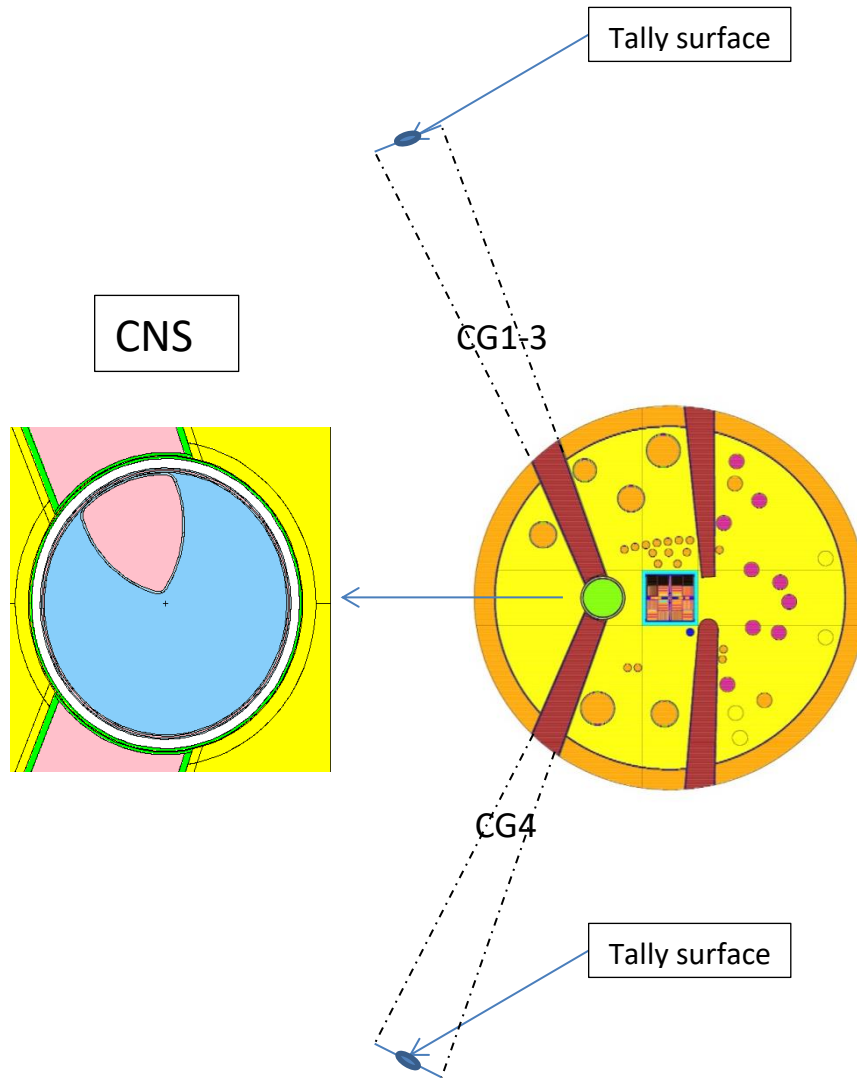


Figure 1

Figure A-1. Major components of the in-pile assembly showing the flow paths of the helium refrigerant and the liquid deuterium.



**Figure A-2. Model of the CNS adjacent to the reactor core and the cold neutron beam ports. TOF measurements were made at the reactor face - the locations of the Tally surfaces above. The enlarged model of the CNS shows the displacer, filled with cold helium gas, serving as a reentrant hole to enhance the cold neutron flux in the direction of CG 1-3.**

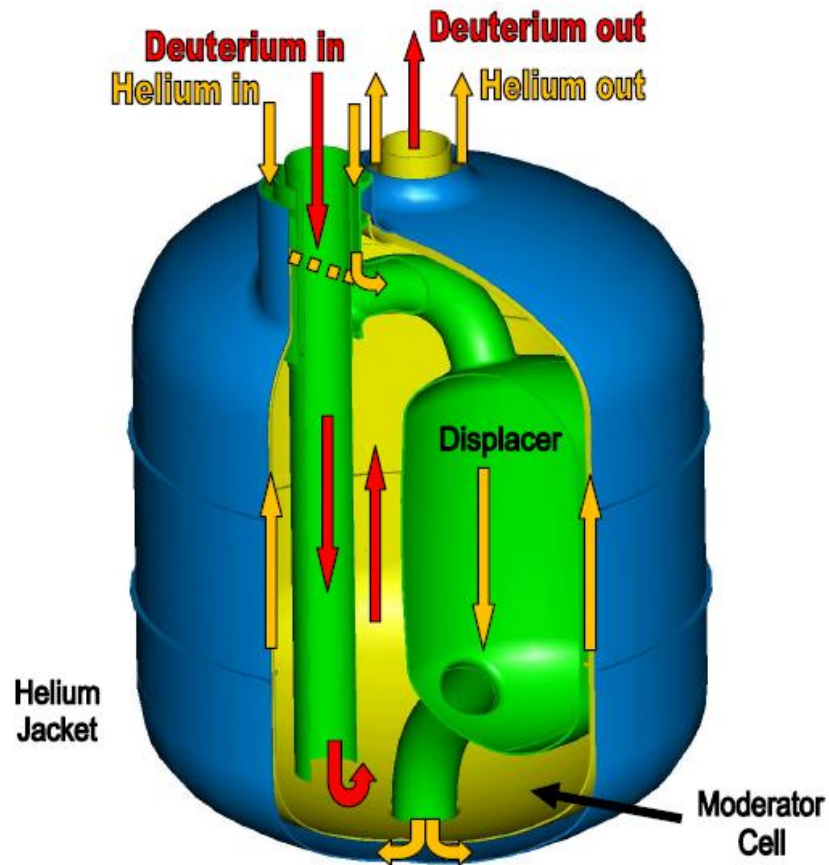


Figure A-3. Details of the moderator cell, showing the Displacer and the helium refrigerant flow pattern through it and the jacket surrounding the cell.

#### Proposed CNS Design Changes:

Any changes in the design of the Mark II CNS are subject to many constraints imposed by the geometry of the heavy water reflector tank. The new in-pile assembly must be installed in the existing Zircaloy vacuum jacket and must be connected to a flange at its top. Thus the diameter, elevation, and total height of the in-pile are fixed. The proposed options are shown in Figure A-4: Case 1 is the existing source; Case 2 is the removal of the displacer from the existing geometry; Case 3 is to increase the height of the existing source by 7 cm (~ 5 additional liters of LD<sub>2</sub>); and Case 4 includes both extending the height 7 cm and removing the displacer [2]. Given the constraints imposed by the fixed geometry (the depth and diameter of the Zircaloy vacuum jacket), these are a reasonable set of options to consider. Other moderators, such as liquid hydrogen were rejected by INVAP in the design stage of OPAL. (A liquid hydrogen source would need to be supercritical, requiring a much more complicated cryogenic cooling

system. A mixture of LD2 and LH2 may be difficult to realize owing to differing boiling points, and the production of HD molecules. There are no alternative moderators.)

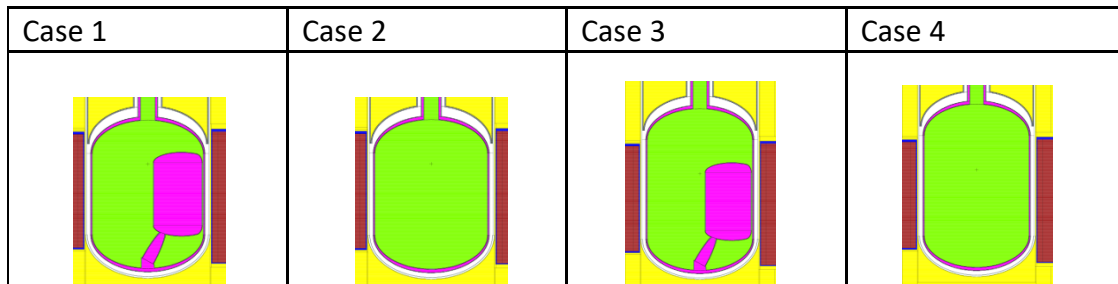


Figure A-4. Proposed changes to the geometry of the OPAL cold source. Case 1 is the existing source.

**Neutronics:**

The ANSTO Nuclear Analysis Section (NAS) has very good models of OPAL and the CNS, and the transport codes and data to analyze these proposals. They have been used to benchmark measurements of the absolute flux spectrum at the reactor face on CG1 with good agreement [1]. The calculations follow a three-step process: (1) a lengthy full core MCNP criticality calculation generates a surface source file containing the energy, position, and direction of the neutrons entering the CNS and beam ports in the reflector tank, (2) the surface source is used to generate starting particles for second MCNP calculation of the current of neutrons at the entrance of CG1, exploiting the DXTRAN variance reduction tool to build good tally statistics, and (3) a GTRANS6 neutron optics calculation of the flux at the end of CG1 that correctly models the geometry and reflectivity of the guide. Steps (1) and (2) are exactly the procedures used at NIST to calculate CNS gains. Step (3) is needed to correctly transport the neutrons through guide CG1, and indicative of the gains to be expected at the instruments. Data needed for input to GTRANS6 is obtained from the DXTRAN tallies using the PTRAC feature of MCNP because the code cannot write a surface source for the DXTRAN “pseudo particles”. Step 3 is also needed to compare the model to the TOF measurements of the flux spectrum exiting CG1 at the reactor face.

The results of the benchmark efforts for CG1 are shown in Figure A-5. The agreement for cold neutrons, energy below 5 meV, is very good. The calculations also yield the correct gains, NO/SO, based on measurements on 4 instruments in the guide hall as shown in Figure A-6. These results have verified and validated the NAS models and their use of these analysis tools.



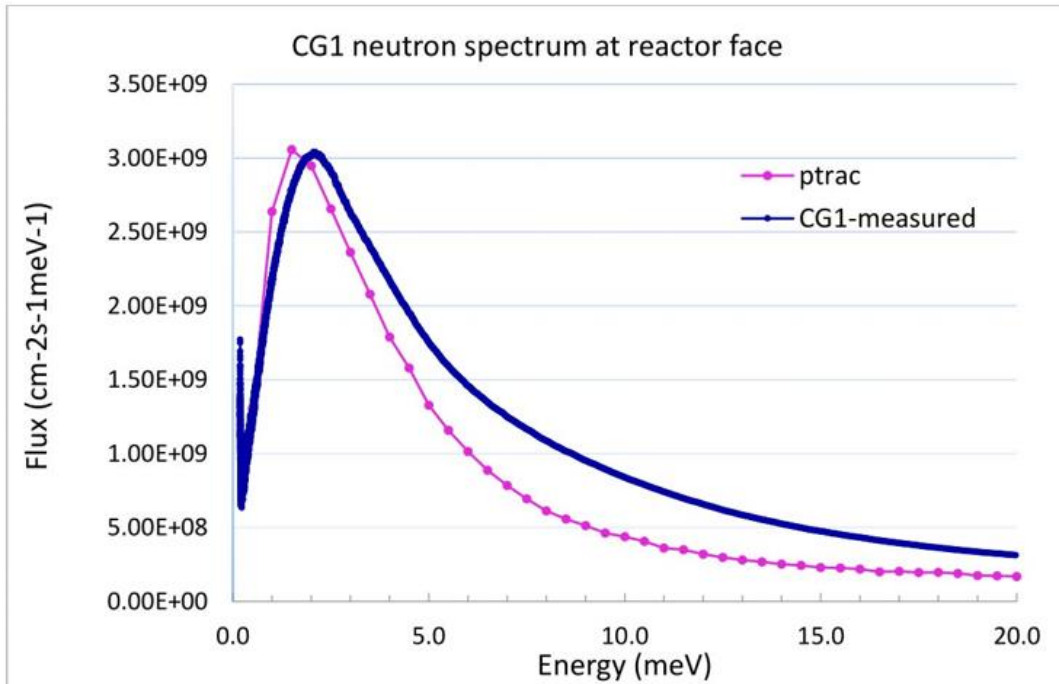


Figure A-5. Calculated (ptrac) vs. measured flux spectrum at CG1.

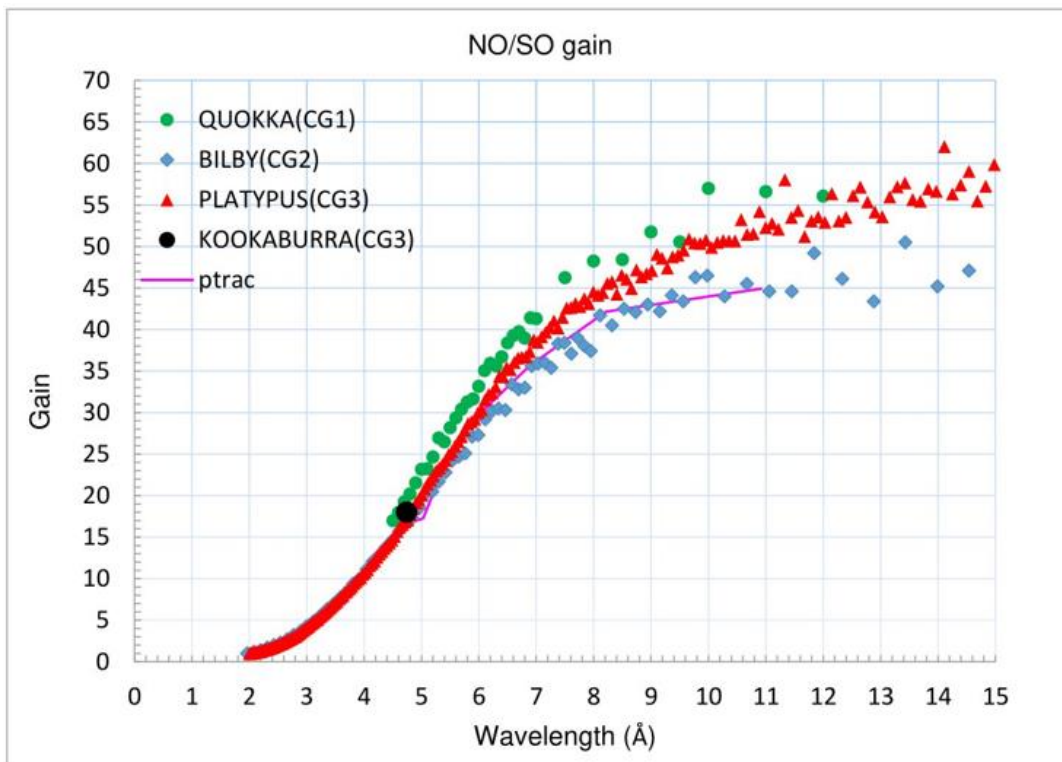


Figure A-6. Calculated CNS gain (ptrac) vs. measured cold neutron gains NO/SO at various instruments in the guide hall.

The relative performance of the three options with respect to the existing source is shown in Figure A-7 below. These plots clearly show that there is quite a penalty for removing the displacer, eliminating Cases 2 and 4. Case 3, on the other hand, simply has more moderator in a high neutron flux, and offers modest cold neutron gains over the range of wavelengths of most use to the scattering instruments in the guide hall. The additional LD<sub>2</sub> is not in the plane of the beam ports, however, as there is no room. A separate parametric study on the shape of the reentrant hole was also performed [3]. After calculating the CG1 flux for 9 cavity variations of width and/or depth, it was concluded the original hole geometry is optimum, and any change would adversely affect some portion of the spectrum.

The displacer was installed to optimize the cold neutron flux in CG1-3, at the expense of somewhat poorer performance at CG4. Since there is a desire in the Bragg Institute to eventually build a second guide hall that would use the CG4 beam port for new guides, one might reasonably ask if now is the time to modify the CNS to balance the flux in each direction by perhaps including two shallow displacers facing each direction. This was not done for three solid reasons: (1) the goals for a second guide hall are not established, (2) such a modification to the CNS would significantly complicate its internal structure and fabrication, and (3) the gains are very modest, not worth the trouble. A better strategy would be to follow the example of NCMR [4] or ILL [5] when the time comes for a new guide hall, which is to identify the desired new or improved instruments and then custom design and build the guides for each instrument.

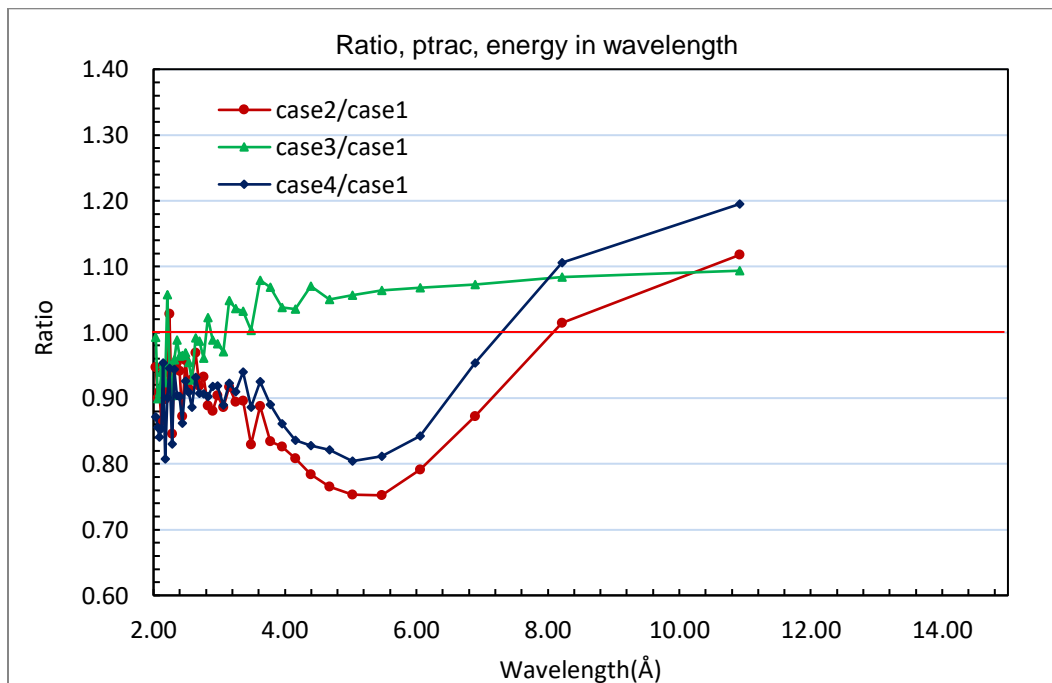
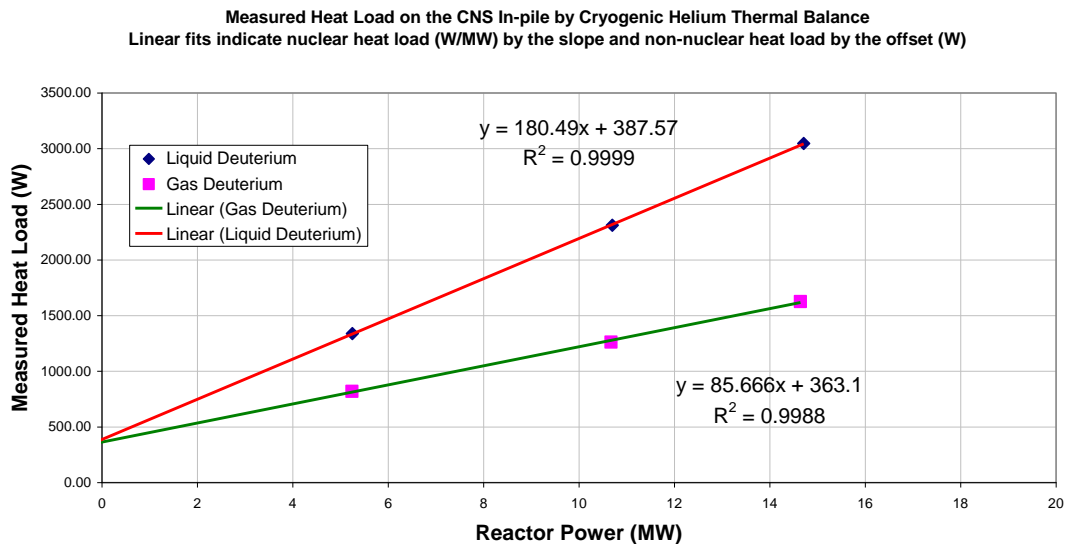


Figure A-7. Relative performance of proposed options for the Mark II CNS as a function of wavelength with respect to the existing source, Case 1.

### **Nuclear Heat Load vs. Refrigerator Capacity:**

The Mark II cold source will be larger than the existing moderator vessel and it will experience more nuclear heating in the additional LD2 and aluminum. The nuclear (and non-nuclear) heat load of the CNS has been carefully measured as a function of reactor power (Figure A-8) in both the NO and SO modes [6,7]. The total heat load is very close to 4000 W in the NO mode, and about 2070 W in the SO mode. These measurements also clearly confirmed that the thermosiphon maintains the deuterium in the liquid phase; raising the He refrigerant temperature above the saturation LD2 saturation temperature (28.3 K at 3.4 bar) results in a noticeable drop in the heat load as LD2 is replaced with some vapor. The upgraded compressor oil heat exchangers have eliminated the earlier problems with the cryogenic plant.



**Figure A-8. Measured heat load on the refrigerator vs. reactor power.**

Heat load measurements must be benchmarked against calculated heat loads to be sure the additional heat load in the LD2 and Al vessel walls for Case 3 can be accommodated. MCNP has been used to estimate the nuclear heating due to neutrons, prompt and delayed (fission products and  $^{28}\text{Al}$ ) gamma rays, and from  $^{28}\text{Al}$  beta particles directly deposited in the vessel walls; the calculations are in excellent agreement with the measurements above. The additional heat load introduced by the Mark II CNS has also been calculated with MCNP to be about 420 W [7]. The cooling capacity of the cryogenic refrigerator has been measured at 6.2 kW with both Compressor A and Compressor B fully loaded to achieve the maximum possible He flow, about 170 g/s [8]. There is no doubt, therefore, that there is an ample reserve of cooling capacity for the Mark II cold source.

### **Thermosiphon Heat Transfer and CFD Models:**

Over the past few years, NAS, with the cooperation of Professor Guan Yeoh and several students, has developed very reliable CFD (Computational Fluid Dynamics) models of the CNS thermosiphon, including both the natural circulation of LD2 between the moderator chamber and the heat exchanger, and the flow of He refrigerant through both components. During the CNS development work, PNPI built a highly instrumented full-scale mockup of the thermosiphon, and the early CFD modeling concentrated on the mockup, shown in Figure A-9. A big part of this modeling effort is the generation of the computational mesh [6] and a mesh with 11 million elements was chosen after testing a finer mesh scheme. The scheme has been tested using two different CFD codes, CFX [9] and STAR-CCM+ [10] and both show good agreement with the PNPI mockup data as seen in Table A-1. The STAR-CCM+ code runs considerably faster and has been adopted by NAS to model the proposed Mark II CNS.

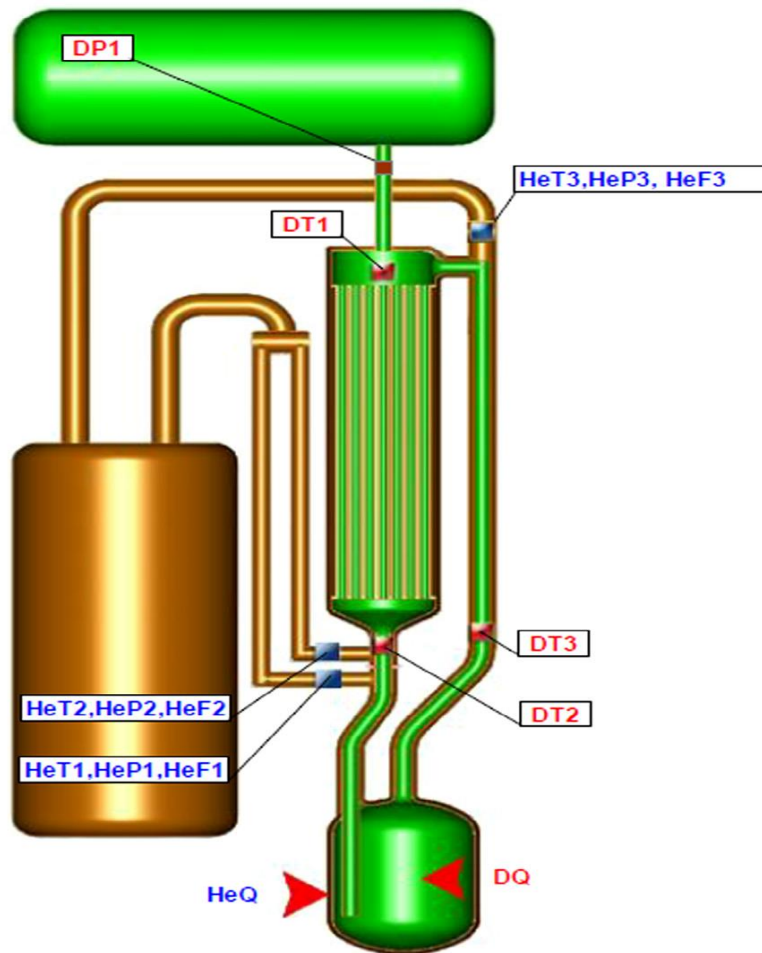


Figure A-9. Schematic of the PNPI mockup of the OPAL cold source, showing the test parameters.

**Table A-1. Comparison of CFD results using CFX and Star-CCM+ with measured parameters [10].**

Parameter	PNPI	CFX	STAR-CCM+
DT1 [K]	25.10	26.00	24.87
DT2-1 [K]	22.00	22.64	22.18
DT3-1 [K]	25.20	26.23	24.87
Tav [K]	23.60	25.21	23.88
HeT1-2 [K]	19.25	19.01	19.83
HeT2-2 [K]	19.00	19.00	19.00
HeT3-2 [K]	24.10	23.98	23.50
DQ [W]	2000	2000	2000
QTot [W]	4000	4200	4200
HeQ [W]	2000	2200	2200
HXHe3 [W]	4300	4208	4170

Both codes have been used to model the existing CNS but there is a more limited data set for comparison. But both calculate the He and LD<sub>2</sub> flow fields everywhere and predict the LD<sub>2</sub> flow (about just over 100 g/s) and the total heat removed by the two He streams. The main benchmark here is the total heat, which agrees very well with the measured value. Preliminary results indicate that the Case 3 proposal will still operate in the subcooled regime [11]. One thing to note is that there is considerable heat transfer through the walls of the displacer. Although Cases 2 and 4 are not now under consideration, it is important to learn whether or not the displacer can simply be replaced by a simple pipe, or if a different scheme is needed. The CFD models and codes have been improved so that they can be confidently used to answer these questions.

**Conclusions:**

The NAS team is to be congratulated for the excellent set of analysis tools they have developed to analyze the performance, heat load, and thermal-hydraulics of the CNS. They have relied on many benchmark measurements to validate the methods. They have applied these tools in the analysis of the proposed Mark II CNS and demonstrated that it will reliably work as expected, and deliver modest gains to the cold neutron scattering instruments [12]. ***I recommend that ANSTO proceed with the detailed design and fabrication of the proposed Mark II In-pile Assembly and continue planning for its installation in 2019.***

I also have a few additional recommendations:

1. The final design review should include an independent mechanical stress analysis and material lifetime estimate.
2. Continue to develop confidence in the nuclear and thermal analysis tools. Seize every opportunity to benchmark the NAS models developed up till now, and in particular, make allowance for flux measurements at CG1, CG4, and scattering instruments after the Mark II source is installed. Repeat the heat load measurements with the new CNS in

both the NO and SO modes at intermediate power levels. These data will further validate the MCNP and CFD models.

3. Expand the collaboration between NIST and ANSTO into engineering. NCNR has gained much experience with our cold moderators over a period of nearly 30 years and is always willing to share our experience with others. We are planning to install a liquid deuterium cold source in the next few years and may need some advice from NAS. Our nuclear analysis group is trying to expand its capabilities in thermal hydraulics simulations (CFD), so this may be another area of common interest. We are also planning to commission a new 7 kW cryogenic plant to accommodate the LD<sub>2</sub> source, and ANSTO personnel are welcome to visit to observe startup and testing.
4. The best way to achieve large gains in the performance of instruments using cold neutrons is to custom-build neutron guides, from the in-pile pieces all the way to the instruments, that deliver the best beam possible to meet the needs of each instrument. If a second guide hall is to be built, ANSTO should adopt this approach after identifying the scientific goals of a new suite of instruments.

In the absence of a major breakthrough in the efforts to develop so-called directed cold moderators (unlikely and fraught with engineering restraints), the Mark II cold source is the best option for the CNS replacement.

#### **References:**

1. Huayou Wu, "Benchmark Calculation methods for CNS spectrum at reactor face", NASDOC RP15-0238 January 2016).
2. Huayou Wu, Weijian Lu, and George Braoudakis, "OPAL CNS Neutronic Benchmarking and Improvement Options", NASDOC RP15-0230 (December 2015).
3. Andrew Pastrello, "Neutron Parametric Study of the Re-entrant Cavity in OPAL Reactor's Cold Neutron Source", NASDOC RP15-0234 (2015).
4. <https://www.ncnr.nist.gov/expansion/guides.html>
5. J. Beaucour, et al, "The H5 guide system – the latest innovative guide system at the ILL", Neutron News, Volume 26, Number 3, 11-14, (2015).
6. Weijian Lu, "The Cold Source Heat Load Measurements", NASDOC RP09-0123 (2009).
7. Tunay Ersez and Weijian Lu, "OPAL CNS Nuclear Heat Load Benchmarking and Parametric Study", NASDOC RP15-0220 (April 2015).
8. Weijian Lu, Memo to David VITTORIO, 29 April 2015.
9. Tom Pavlou, Mark Ho, Guan Heng Yeoh, and Weijian Lu, "Thermal-hydraulic modelling of the Cold Neutron Source thermosiphon system", Ann. Nucl. Erg. 90, pp. 135-147 (2016).
10. Yeongshin Jeong, "CFD Analysis of CNS Thermosiphon Loop Using STAR-CCM+", NASDOC RP15-0215 (2014).

11. James Spedding, "OPAL CNS CFD Analysis with Star-CCM+", RP16-0242 (March 2016).
12. Weijian Lu, "Options Study NASDOC RP15-0219.

## Appendix B - A preliminary analysis of the effect of CNS location on brightness, signal-to-noise ratio, and heat load (Authored by: Danyal J. Turkoglu)

### Background and Introduction

A replacement reactor at the NCNR would, ideally, be optimized for cold neutron science because most experiments at the NCNR use cold neutrons. Thus far, the figure of merit for evaluating optimality has been brightness ( $\partial^2\phi/\partial\lambda\partial\Omega$ ) for long-wavelength neutrons ( $E_n < 10 \text{ meV}$ ,  $\lambda > 2.96 \text{ \AA}$ ) in the direction of the beam or neutron guides, which correlates with signal strength and counting times for instruments. Brightness, being wavelength-dependent, can be used directly in simulations of instrument performance involving neutron optics (neutron guides and filters). Neutron optics can conserve the brightness of long-wavelength neutrons while reducing the beam content of short-wavelength neutrons and gamma rays that may degrade the signal-to-noise ratio (SNR). If SNR were used as a figure of merit, evaluating SNR should involve tailoring neutron optics for individual instruments based on their requirements and susceptibility to noise.

As a preliminary study to understand potential gains that might be realized from a replacement reactor, a simplified preliminary NNS neutronics model is used, referred to informally as Box9. For a fair comparison, the guides and filters were kept constant, and the following parameters were kept roughly the same between the two models: in-pile guide size (6 cm width  $\times$  20 cm height) and distance from CNS to guides (1.5 m). While the gains in cold neutron flux from the Box9 source were more than a factor of 2 higher than the NBSR LD<sub>2</sub>, the results suggested that SNR – defined in this study as the  $\phi_{slow}(\lambda > 1 \text{ \AA})/\phi_{non-slow}(\lambda < 1 \text{ \AA})$  – was worse for the Box9 model.

In this work, the location of the north LD<sub>2</sub> CNS was evaluated in four locations, as shown in Figure B-1, in terms of brightness and compared to the NBSR LH<sub>2</sub> CNS (Unit 2) and NBSR LD<sub>2</sub> CNS (Unit 3, expected installation in 2023). As shown in Figure B-2, the neutron guides (NGs) were kept 1.5 m from the CNS center. NG-5, in the central position, was used for the brightness tally in MCNP6. Note that this is a scoping analysis based on a rough model of the NNS, and it is not fully representative of the reactor or facility geometry.

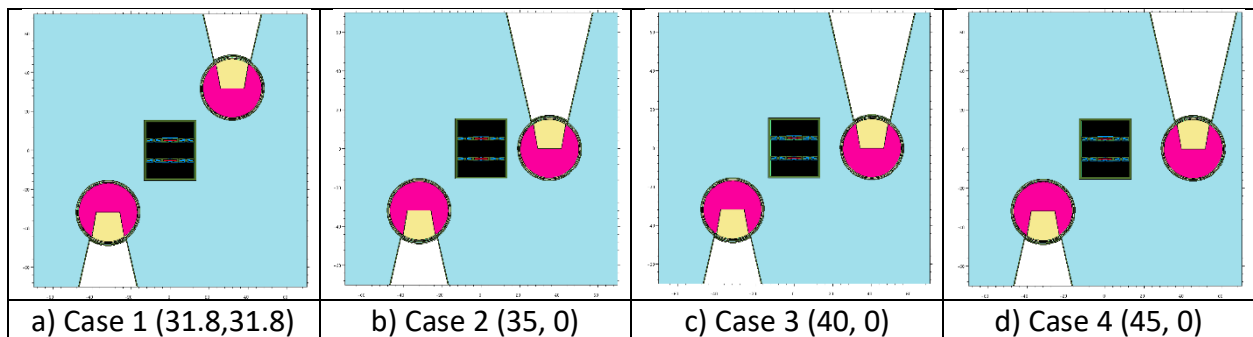


Figure B-1. Plan-view schematics of the four cases showing the varying position of the north LD<sub>2</sub> CNS in the middle-of-cycle Box9 model. The ordered pair in parentheses is the (x,y) location of the CNS center.



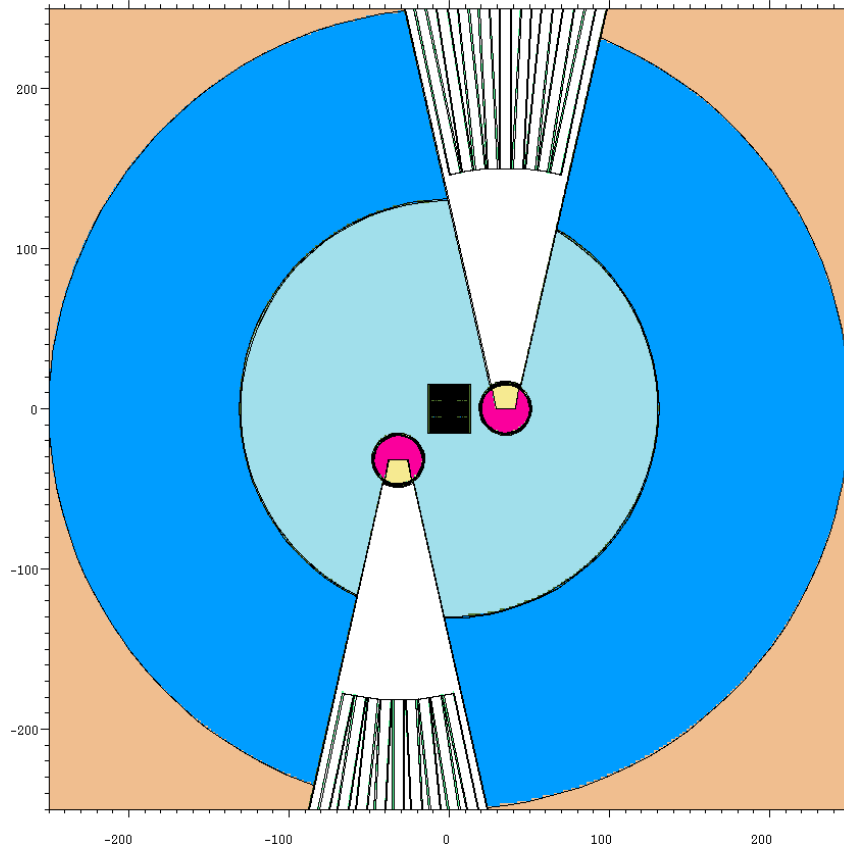


Figure B-2. Plan-view schematic of Case 2 showing the distance (1.5 m) of the neutron guides from the CNS center.

## Results

The brightness for the four Box9 cases and the two NBSR cases are shown in Figure B-3 with logarithmic scales and in Figure B-4 with linear scales. For the Box9 cases with the CNS on the side of the core (Cases 2-4), the brightness increases for all wavelengths as the CNS moves closer to the core. Case 1, with the CNS at the default corner location, has comparable performance to Case 4 at the furthest position from the core on the side.

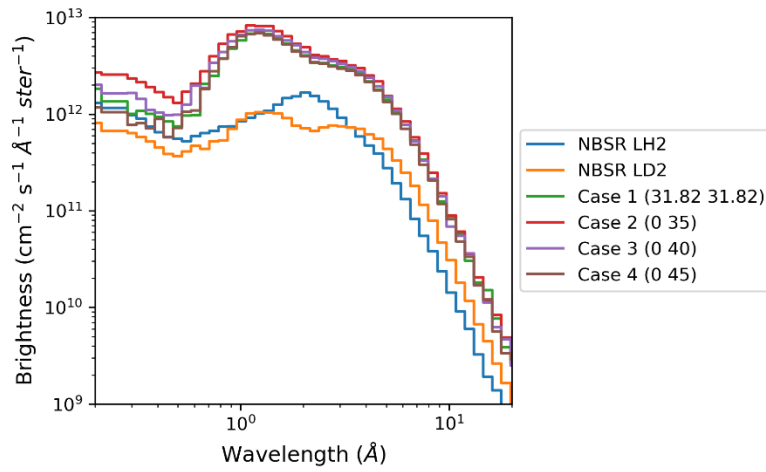


Figure B-3. Comparison of brightness with logarithmic scales.

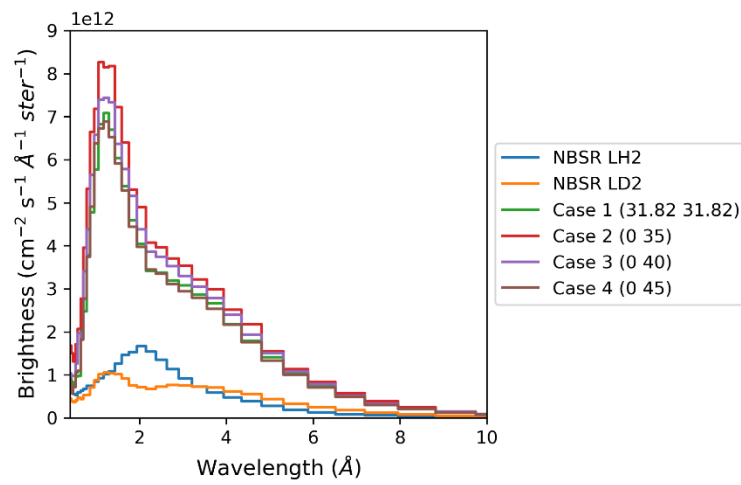


Figure B-4. Comparison of brightness with linear scales.

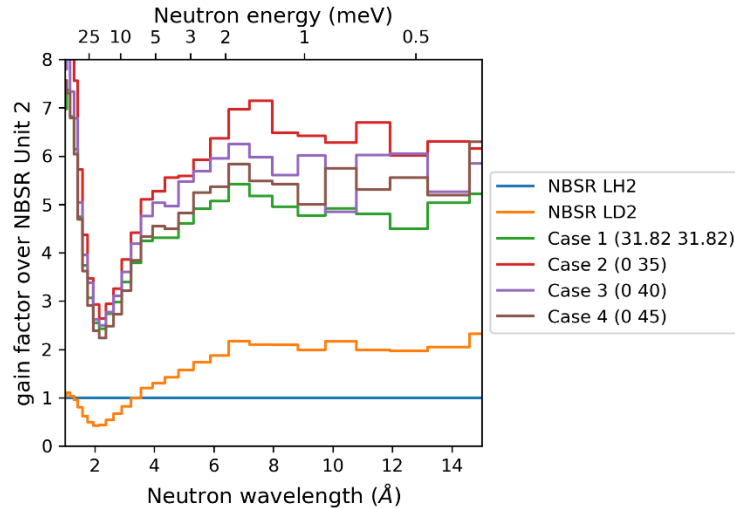


Figure B-5. Comparison of brightness gain factors of NBSR LH2.

The brightness results are summarized in Figure B-5 and Table B-1 where the following is true.

- Integrated brightness for cold, slow, and non-slow neutrons was calculated by integrating brightness
- Fractions of neutrons,  $F_{cold}$  and  $F_{slow}$ , were calculated as the ratio of the particular brightness to the total brightness
- SNR was calculated as the slow-neutron brightness to the non-slow-neutron brightness.

These results again indicate that moving the CNS closer to the core increases cold neutron brightness at the expense of SNR. The corner location of Case 1 performed better than the further side location of Case 4 in terms of cold neutron brightness, but it was worse in terms of SNR.

Table B-1. Summary of brightness results.

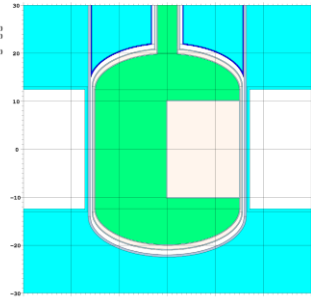
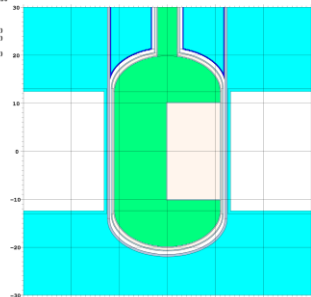
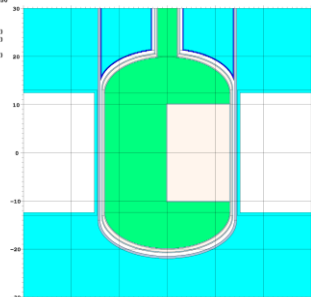
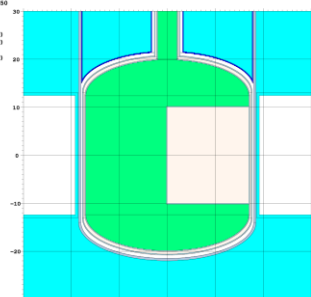
CNS	Position	Integrated brightness ( $\times 10^{12} \text{ cm}^{-2}\text{s}^{-1}\text{ster}^{-1}$ )				$F_{cold}$	$F_{slow}$	SNR
		Cold ( $\lambda > 2.9 \text{ \AA}$ )	Slow ( $\lambda > 0.96 \text{ \AA}$ )	Non-slow ( $\lambda < 0.96 \text{ \AA}$ )	Total			
NBSR LH2	n/a	2.2	4.7	2.1	6.8	0.32	0.69	2.2
NBSR LD2	n/a	2.7	4.3	1.3	5.6	0.48	0.77	3.3
Case 1	(31.82, 31.82)	9.5	19.1	3.0	22.1	0.43	0.87	6.4
Case 2	(0, 35)	10.7	22.3	5.9	28.3	0.38	0.79	3.8
Case 3	(0, 40)	10.0	20.6	3.6	24.2	0.41	0.85	5.7
Case 4	(0, 45)	9.1	18.7	2.3	20.9	0.43	0.89	8.2

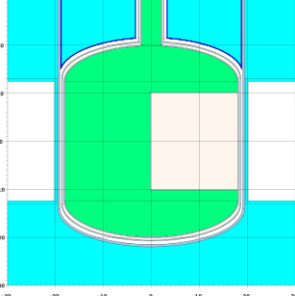
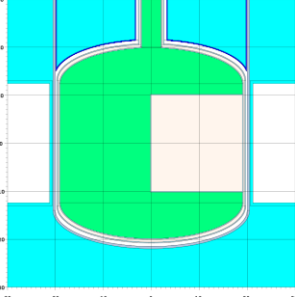
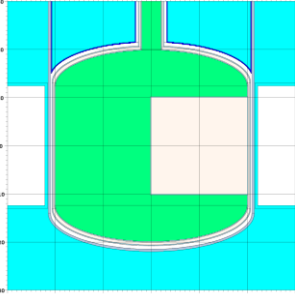
Lastly, moving the CNS closer to the core for increased brightness comes at the expense of increased nuclear heat load. Table B-2 compares nuclear heat loads for the four cases. A constraint in the cold source design, including its location, is that the nuclear heat load should be less than 4 kW to enable the use of passive heat removal via natural circulation (thermosiphon). The heat loads of Cases 2 and 3 appear to violate this constraint. However, the current design of the CNS has an extra aluminum shell as the design is copied from the OPAL reactor CNS design that employs subcooled LD<sub>2</sub> with cold helium removing heat directly from the cryostat. Thus, it's likely that these are conservative upper bounds for the heat loads.

**Table B-2. Nuclear heat load results for the four Box9 cases.**

Case		Deuterium		Aluminum			Total
		Neutron	Gamma	Neutron	Gamma	Beta	
Case 1	(31.82, 31.82)	722	597	10	934	1686	3950
Case 2	(0, 35)	2706	1082	40	1538	1949	7315
Case 3	(0, 40)	1189	788	18	1174	1812	4982
Case 4	(0, 45)	520	588	8	927	1645	3688

### Appendix C - A visual of all NNS CNS diameters investigated in this work

NNS CNS Diameter	
<p style="text-align: center;"> <math>\varnothing</math> 30 cm                      (current powr_Box9_v02_SU_c7_guides model)                 </p>	<pre> 09/16/21 08:54:14 powr_Box9_v02_SU_c7_guides =   Full: All guides Box9 v0.2 1350   Fuel: C2 UraniumPKA   problem = 09/16/21 14:31:15   kernel: 18   ( 0.00000, 1.00000, 0.00000)   ( 0.00000, 0.00000, 1.00000)   origin:   ( 45.00, 0.00, 0.00)   extent = ( 30.00, 30.00)                     </pre> 
<p style="text-align: center;"> <math>\varnothing</math> 22 cm                 </p>	<pre> 09/14/21 14:10:35 powr_Box9_v02_SU_c7_guides_CM02 =   Full: CNS 4x22cm   problem = 09/14/21 15:25:35   kernel: 18   ( 0.00000, 1.00000, 0.00000)   ( 0.00000, 0.00000, 1.00000)   origin:   ( 45.00, 0.00, 0.00)   extent = ( 30.00, 30.00)                     </pre> 
<p style="text-align: center;"> <math>\varnothing</math> 26 cm                 </p>	<pre> 09/14/21 15:19:55 powr_Box9_v02_SU_c7_guides_CM04 =   Full: All guides Box9 v0.2 1350   Fuel: CNS 4x26cm   problem = 09/14/21 15:26:11   kernel: 18   ( 0.00000, 1.00000, 0.00000)   ( 0.00000, 0.00000, 1.00000)   origin:   ( 45.00, 0.00, 0.00)   extent = ( 30.00, 30.00)                     </pre> 
<p style="text-align: center;"> <math>\varnothing</math> 34 cm                 </p>	<pre> 09/14/21 14:09:35 powr_Box9_v02_SU_c7_guides_CM04 =   Full: All guides Box9 v0.2 1350   Fuel: CNS 4x34cm   problem = 09/14/21 15:26:29   kernel: 18   ( 0.00000, 1.00000, 0.00000)   ( 0.00000, 0.00000, 1.00000)   origin:   ( 45.00, 0.00, 0.00)   extent = ( 30.00, 30.00)                     </pre> 

<p style="text-align: center;">∅ 36 cm</p>	<pre> 09/14/21 08:23:11 pwr_bench_v01_01_07_01_guides_0816 = 4113 Al guidelines Rev9 v0.2 1390 Fuel_CMO de-floc problem = 09/13/21 14:09:14 material: 18 ( 0.000000, 1.000000, 0.000000) ( 0.000000, 0.000000, 1.000000) origin: ( 45.00, 0.00, 0.00) axismat = ( 30.00, 30.00)           </pre> 
<p style="text-align: center;">∅ 38 cm</p>	<pre> 09/14/21 14:10:14 pwr_bench_v01_01_07_01_guides_0818 = 4113 Al guidelines Rev9 v0.2 1390 Fuel_CMO de-floc problem = 09/14/21 15:26:51 material: 18 ( 0.000000, 1.000000, 0.000000) ( 0.000000, 0.000000, 1.000000) origin: ( 45.00, 0.00, 0.00) axismat = ( 30.00, 30.00)           </pre> 
<p style="text-align: center;">∅ 40 cm</p>	<pre> 09/14/21 14:09:10 pwr_bench_v01_01_07_01_guides_0810 = 4113 Al guidelines Rev9 v0.2 1390 Fuel_CMO de-floc problem = 09/14/21 15:27:05 material: 18 ( 0.000000, 1.000000, 0.000000) ( 0.000000, 0.000000, 1.000000) origin: ( 45.00, 0.00, 0.00) axismat = ( 30.00, 30.00)           </pre> 

## **Appendix D - Specific simulations for NCNR-NNS cold neutron current simulations (Version: October 17, 2022)**

The geometry of the in-pile guides with the future Unit 3 cold neutron source at the NBSR are illustrated in plan view in Figure D-1. It is noted that the present source requires a rather complicated in-pile geometry with in-pile elements that have a common element region before the individual beams split off. Figure D-2. shows the aluminum substrate in-pile element for the central cryogenic beam tube (CTC), to be installed with the LD<sub>2</sub> cold source. In the NNS, with the feasibility of an unrestricted view of the cold source at the guide entrances being possible by design, these complications and common element regions may be eliminated as they give no neutron guide performance advantages. For example, in the NBSR, the CTW guides split off quite far (2.2 m) from the cavity of the cold source. In this case, it was found that pinching the in-pile guide entrance area to fit within the smaller diameter part of the beam tube led to poorer performance for the instruments than having larger area guide entrances further away from the restriction, with slight eclipsing of the corners by the smaller diameter tube. Furthermore, both side cryogenic tubes, CTW and CTE, have axes that do not intersect the brightest portion of the Unit 2 or Unit 3 cold sources. This further restricts the outer body envelope of the in-pile elements because it requires an off-axis alignment of the in-pile. In the NNS, no such restrictions or compromises need apply and it is likely that larger area guides can be arrayed more uniformly with unrestricted optimal view quite close to the source. One factor to consider for the closest approach of the guides is the radiation heating of the guide element. That will be assessed for the NNS guides in conjunction with assessing cooling possibilities for in-pile guide elements (a function currently performed with a He gas flow for the NBSR in-pile guides).

05/14/20 14:15:18  
LD2\_2019\_eocheu\_NG2 LD2 full EOC  
reactor model (NG2 brightness)

probid = 05/14/20 14:10:09  
basis: XY  
( 1.000000, 0.000000, 0.000000)  
( 0.000000, 1.000000, 0.000000)  
origin:  
( -42.40, 205.20, 0.00)  
extent = ( 155.00, 155.00)

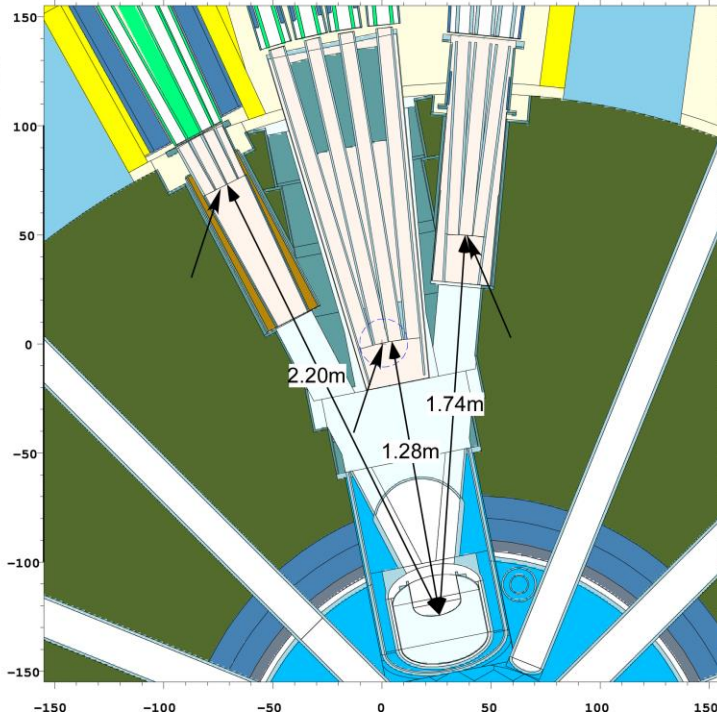


Figure D-1. Geometry of Unit 3 LD2 cold source and in-pile guides from MCNP model.

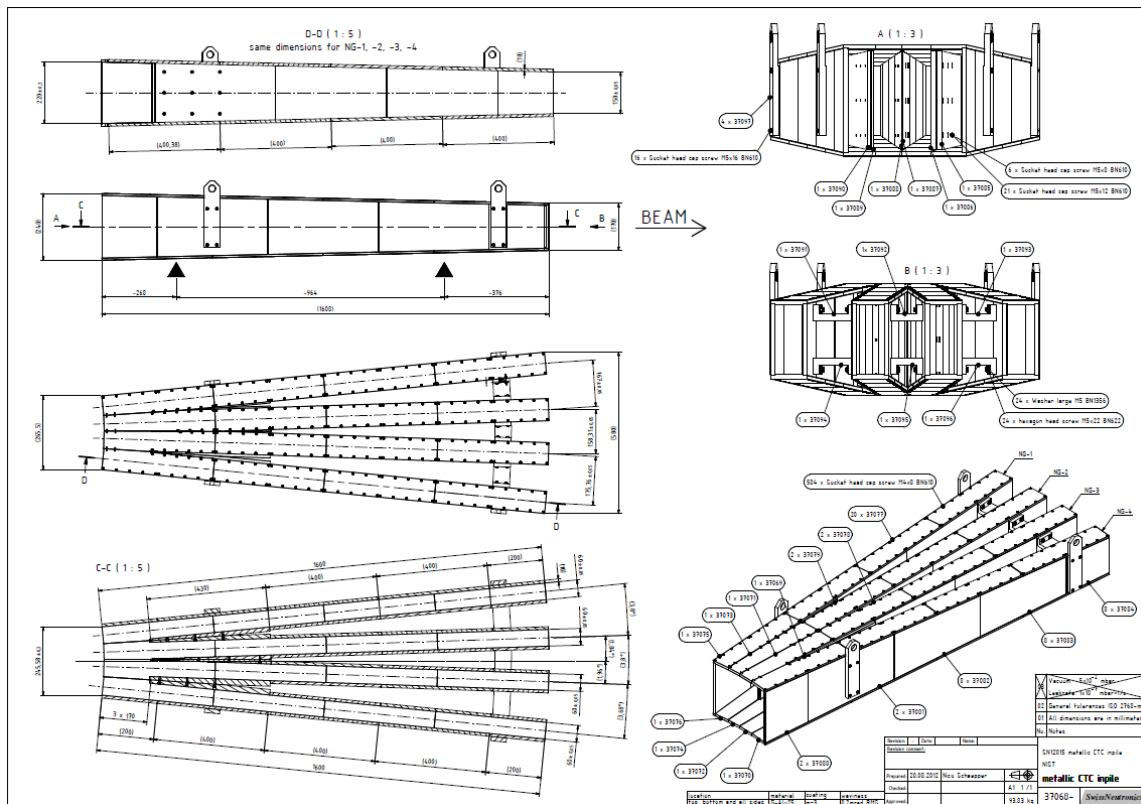


Figure D-2. G1 to 4 in-pile guide replacement to be installed with the LD2 cold source.



**UNIT 2 LH<sub>2</sub> (White beam -all wavelengths NBSR)**

**Table D-1. Integral currents all wavelengths with 2.9° ( $\mu \geq 0.99875$ ) polar angle restriction on entering neutron trajectories (CNS Unit 2).**

Guide	NG1	NG2	NG3	NG4	NG5	NG6	NG7	NGA	NGBI	NGBu	NGC	NGD	TOTAL
$J$ (s <sup>-1</sup> )	3.684E+12	4.456E+12	4.725E+12	4.507E+12	2.199E+12	3.090E+12	1.679E+12	1.519E+12	6.612E+11	6.602E+11	2.216E+12	8.738E+11	3.027E+13
$J_c$ (s <sup>-1</sup> )	5.305E+12	6.381E+12	6.767E+12	6.497E+12	3.157E+12	4.453E+12	2.582E+12	2.242E+12	9.654E+11	9.637E+11	3.241E+12	1.368E+12	4.392E+13
Area guide entrance (cm <sup>2</sup> )	127.44	127.44	127.44	127.44	60.00	90.00	60.00	60.00	25.00	25.00	85.28	36.00	951.04
d (cm)	128	128	128	128	174	174	174	220	220	220	220	220	
Entrance solid angle (sr)	0.0078	0.0078	0.0078	0.0078	0.0020	0.0030	0.0020	0.0012	0.0005	0.0005	0.0018	0.0007	0.0428
$\lambda\lambda\bar{n}$ (Å)	2.59	2.57	2.58	2.59	2.58	2.59	2.76	2.65	2.63	2.62	2.63	2.82	2.61

**Table D-2. Integral currents all wavelengths with 5.2° ( $\mu \geq 0.99595$ ) polar angle restriction on entering neutron trajectories (CNS Unit 2).**

Guide	NG1	NG2	NG3	NG4	NG5	NG6	NG7	NGA	NGBI	NGBu	NGC	NGD	TOTAL
$J$ (s <sup>-1</sup> )	8.145E+12	8.848E+12	8.977E+12	8.676E+12	2.812E+12	4.178E+12	2.145E+12	1.654E+12	7.289E+11	7.279E+11	2.537E+12	9.506E+11	5.038E+13
$J_c$ (s <sup>-1</sup> )	1.174E+13	1.268E+13	1.287E+13	1.251E+13	4.046E+12	6.024E+12	3.305E+12	2.445E+12	1.065E+12	1.063E+12	3.723E+12	1.501E+12	7.296E+13
$\lambda\lambda\bar{n}$ (Å)	2.59	2.58	2.58	2.59	2.59	2.59	2.77	2.66	2.63	2.63	2.64	2.84	2.60

**Table D-3. Integral currents all wavelengths with NO polar angle restriction on entering neutron trajectories (CNS Unit 2).**

Guide	NG1	NG2	NG3	NG4	NG5	NG6	NG7	NGA	NGBI	NGBu	NGC	NGD	TOTAL
$J$ (s <sup>-1</sup> )	1.043E+13	1.076E+13	1.076E+13	1.044E+13	2.812E+12	4.187E+12	2.145E+12	1.654E+12	7.289E+11	7.279E+11	2.537E+12	9.506E+11	5.813E+13
$J_c$ (s <sup>-1</sup> )	1.505E+13	1.542E+13	1.542E+13	1.505E+13	4.047E+12	6.038E+12	3.305E+12	2.445E+12	1.065E+12	1.063E+12	3.724E+12	1.501E+12	8.413E+13
$\lambda\lambda\bar{n}$ (Å)	2.59	2.58	2.58	2.59	2.59	2.59	2.77	2.66	2.63	2.63	2.64	2.84	2.60

**UNIT 2 LH<sub>2</sub> ( $\lambda \geq 4\text{Å}$  NBSR)**

**Table D-4. Integral currents for  $\lambda > 4\text{Å}$  with 2.9° ( $\mu \geq 0.99875$ ) polar angle restriction on entering neutron trajectories (CNS Unit 2).**

Guide	NG1	NG2	NG3	NG4	NG5	NG6	NG7	NGA	NGBI	NGBu	NGC	NGD	TOTAL
$J$ (s <sup>-1</sup> )	7.629E+11	9.132E+11	9.681E+11	9.341E+11	4.496E+11	6.404E+11	3.748E+11	3.274E+11	1.397E+11	1.399E+11	4.722E+11	2.121E+11	6.334E+12
$J_c$ (s <sup>-1</sup> )	2.547E+12	3.044E+12	3.227E+12	3.124E+12	1.519E+12	2.141E+12	1.260E+12	1.114E+12	4.719E+11	4.724E+11	1.590E+12	7.296E+11	2.124E+13
$\lambda\lambda\bar{n}$ (Å)	6.00	5.99	5.99	6.01	6.08	6.01	6.04	6.12	6.07	6.07	6.06	6.18	6.03

**Table D-5. Integral currents for  $\lambda > 4\text{Å}$  with 5.2° ( $\mu \geq 0.99595$ ) polar angle restriction on entering neutron trajectories (CNS Unit 2).**

Guide	NG1	NG2	NG3	NG4	NG5	NG6	NG7	NGA	NGBI	NGBu	NGC	NGD	TOTAL
$J$ (s <sup>-1</sup> )	1.688E+12	1.814E+12	1.841E+12	1.797E+12	5.755E+11	8.651E+11	4.792E+11	3.565E+11	1.538E+11	1.539E+11	5.410E+11	2.324E+11	1.050E+13
$J_c$ (s <sup>-1</sup> )	5.651E+12	6.053E+12	6.142E+12	6.016E+12	1.953E+12	2.899E+12	1.617E+12	1.217E+12	5.206E+11	5.207E+11	1.836E+12	8.081E+11	3.523E+13
$\lambda\lambda\bar{n}$ (Å)	6.02	6.00	6.00	6.02	6.10	6.03	6.07	6.14	6.09	6.09	6.10	6.25	6.04

**Table D-6. Integral currents for  $\lambda > 4\text{\AA}$  with NO polar angle restriction on entering neutron trajectories (CNS Unit 2).**

Guide	NG1	NG2	NG3	NG4	NG5	NG6	NG7	NGA	NGBI	NGBu	NGC	NGD	TOTAL
$J$ ( $\text{s}^{-1}$ )	2.162E+12	2.206E+12	2.206E+12	2.162E+12	5.755E+11	8.671E+11	4.792E+11	3.565E+11	1.538E+11	1.539E+11	5.411E+11	2.324E+11	1.209E+13
$J_c$ ( $\text{s}^{-1}$ )	7.242E+12	7.367E+12	7.365E+12	7.241E+12	1.953E+12	2.906E+12	1.617E+12	1.217E+12	5.206E+11	5.207E+11	1.836E+12	8.082E+11	4.059E+13
$\lambda\lambda\bar{n}$ ( $\text{\AA}$ )	6.02	6.01	6.01	6.02	6.10	6.03	6.07	6.14	6.09	6.09	6.10	6.25	6.04

### UNIT 3 LD2 (White beam – all wavelengths NBSR)

**Table D-7. Integral currents for all wavelengths with  $2.9^\circ$  ( $\mu \geq 0.99875$ ) polar angle restriction on entering neutron trajectories (CNS Unit 3).**

Guide	NG1	NG2	NG3	NG4	NG5	NG6	NG7	NGA	NGBI	NGBu	NGC	NGD	TOTAL
$J$ ( $\text{s}^{-1}$ )	5.678E+12	5.684E+12	5.684E+12	5.492E+12	2.497E+12	3.906E+12	2.496E+12	2.010E+12	9.588E+11	9.579E+11	3.364E+12	1.166E+12	3.989E+13
$J_c$ ( $\text{s}^{-1}$ )	1.025E+13	1.021E+13	1.020E+13	9.946E+12	4.565E+12	7.052E+12	4.564E+12	3.730E+12	1.760E+12	1.758E+12	6.161E+12	2.299E+12	7.249E+13
$\lambda\lambda\bar{n}$ ( $\text{\AA}$ )	3.24	3.23	3.23	3.26	3.29	3.25	3.29	3.34	3.30	3.30	3.29	3.55	3.27

**Table D-8. Integral currents for all wavelengths with  $5.2^\circ$  ( $\mu \geq 0.99595$ ) polar angle restriction on entering neutron trajectories (CNS Unit 3).**

Guide	NG1	NG2	NG3	NG4	NG5	NG6	NG7	NGA	NGBI	NGBu	NGC	NGD	TOTAL
$J$ ( $\text{s}^{-1}$ )	1.780E+13	1.834E+13	1.834E+13	1.726E+13	7.531E+12	1.237E+13	7.530E+12	4.755E+12	2.437E+12	2.435E+12	8.449E+12	2.760E+12	1.200E+14
$J_c$ ( $\text{s}^{-1}$ )	3.218E+13	3.295E+13	3.298E+13	3.125E+13	1.375E+13	2.231E+13	1.375E+13	8.784E+12	4.456E+12	4.450E+12	1.550E+13	5.454E+12	2.178E+14
$\lambda\lambda\bar{n}$ ( $\text{\AA}$ )	3.25	3.23	3.23	3.26	3.28	3.24	3.28	3.32	3.29	3.29	3.30	3.55	3.26

**Table D-9. Integral currents for all wavelengths with NO polar angle restriction on entering neutron trajectories (CNS Unit 3).**

Guide	NG1	NG2	NG3	NG4	NG5	NG6	NG7	NGA	NGBI	NGBu	NGC	NGD	TOTAL
$J$ ( $\text{s}^{-1}$ )	5.114E+13	5.668E+13	5.670E+13	5.116E+13	1.256E+13	2.108E+13	1.252E+13	5.395E+12	2.892E+12	2.891E+12	1.012E+13	3.121E+12	2.863E+14
$J_c$ ( $\text{s}^{-1}$ )	9.242E+13	1.019E+14	1.020E+14	9.246E+13	2.292E+13	3.804E+13	2.285E+13	9.979E+12	5.286E+12	5.280E+12	1.863E+13	6.223E+12	5.179E+14
$\lambda\lambda\bar{n}$ ( $\text{\AA}$ )	3.25	3.23	3.23	3.25	3.28	3.25	3.28	3.33	3.29	3.28	3.31	3.59	3.25

### UNIT 3 LD<sub>2</sub> ( $\lambda \geq 4\text{\AA}$ NBSR)

**Table D-10. Integral currents for  $\lambda > 4\text{\AA}$  with  $2.9^\circ$  ( $\mu \geq 0.99875$ ) polar angle restriction on entering neutron trajectories (CNS Unit 3).**

Guide	NG1	NG2	NG3	NG4	NG5	NG6	NG7	NGA	NGBI	NGBu	NGC	NGD	TOTAL
$J$ ( $\text{s}^{-1}$ )	1.919E+12	1.911E+12	1.909E+12	1.864E+12	8.593E+11	1.322E+12	8.590E+11	7.008E+11	3.312E+11	3.303E+11	1.160E+12	4.437E+11	1.361E+13
$J_c$ ( $\text{s}^{-1}$ )	6.838E+12	6.805E+12	6.795E+12	6.666E+12	3.080E+12	4.720E+12	3.080E+12	2.546E+12	1.194E+12	1.190E+12	4.163E+12	1.633E+12	4.871E+13
$\lambda\lambda\bar{n}$ ( $\text{\AA}$ )	6.41	6.40	6.40	6.43	6.45	6.42	6.45	6.53	6.48	6.48	6.45	6.62	6.44

**Table D-11. Integral currents for  $\lambda > 4\text{\AA}$  with  $5.2^\circ$  ( $\mu \geq 0.99595$ ) polar angle restriction on entering neutron trajectories (CNS Unit 3).**

Guide	NG1	NG2	NG3	NG4	NG5	NG6	NG7	NGA	NGBI	NGBu	NGC	NGD	TOTAL
$J$ ( $\text{s}^{-1}$ )	6.018E+12	6.173E+12	6.167E+12	5.840E+12	2.575E+12	4.176E+12	2.573E+12	1.637E+12	8.333E+11	8.324E+11	2.896E+12	1.031E+12	4.075E+13
$J_c$ ( $\text{s}^{-1}$ )	2.152E+13	2.200E+13	2.198E+13	2.091E+13	9.264E+12	1.492E+13	9.259E+12	5.957E+12	3.010E+12	3.004E+12	1.048E+13	3.875E+12	1.462E+14
$\lambda\lambda\bar{n}$ ( $\text{\AA}$ )	6.43	6.41	6.41	6.44	6.47	6.43	6.47	6.54	6.50	6.49	6.50	6.76	6.45

**Table D-12. Integral currents for  $\lambda > 4\text{\AA}$  with NO polar angle restriction on entering neutron trajectories (CNS Unit 3).**

Guide	NG1	NG2	NG3	NG4	NG5	NG6	NG7	NGA	NGBI	NGBu	NGC	NGD	TOTAL
$J$ ( $\text{s}^{-1}$ )	1.725E+13	1.904E+13	1.904E+13	1.725E+13	4.278E+12	7.110E+12	4.267E+12	1.856E+12	9.868E+11	9.857E+11	3.466E+12	1.167E+12	9.671E+13
$J_c$ ( $\text{s}^{-1}$ )	6.178E+13	6.794E+13	6.794E+13	6.178E+13	1.542E+13	2.543E+13	1.539E+13	6.772E+12	3.567E+12	3.560E+12	1.260E+13	4.439E+12	3.466E+14
$\Delta\lambda/\lambda$ ( $\text{\AA}$ )	6.44	6.42	6.42	6.44	6.48	6.43	6.48	6.56	6.50	6.49	6.54	6.84	6.45